J. Fluid Mech. (2001), *vol.* 443, *pp.* 27–68. Printed in the United Kingdom

Transverse jets and jet flames. Part 2. Velocity and OH field imaging

By E. F. HASSELBRINK JR† AND M. G. MUNGAL

Department of Mechanical Engineering, Stanford University, Stanford, CA 94305-3032, USA

(Received 13 September 2000 and in revised form 30 January 2001)

Detailed measurements of the velocity field in the symmetry plane of two jets and two jet flames in a crossflow are obtained using particle image velocimetry. The jets issue into a wind tunnel at density-weighted jet-to-crossflow velocity ratios $r = 10$ and $r = 21$, with corresponding Reynolds numbers 6000 and 12 800. Ensemble statistics of the velocity field are presented, and some interesting features of the entrainment process in transverse jets are discussed. Deviations from the simple behaviour predicted by the similarity analysis presented in Part 1 are highlighted. Simultaneous planar laser-induced fluorescence imaging of the OH radical is performed in selected regions of the flames. Results suggests that flame/flow interaction is strong near the lifted flamebase, but increasingly weaker further downstream.

1. Introduction

Part 1 of this study (Hasselbrink & Mungal 2001), presented a similarity theory and scaling laws for velocity and scalar averages/fluctuations for transverse jets, and demonstrated agreement with existing data. This work presents experimental results, focused on three topics:

(*a*) Detailed investigation of the velocity field in the symmetry plane of transverse jets. Detailed velocity and vorticity field measurements in the counter-rotating vortex pair (CVP) cross-section have been performed by several investigators (Kamotani & Greber 1972; Fearn & Weston 1974; Moussa, Trischka & Eskinazi 1977; Kuzo 1995) for jets with blowing ratios as high as $r = 20$, where r is defined as the square root of the jet-to-crossflow momentum flux ratio. Other studies (Coelho & Hunt 1989; Kelso, Lim & Perry 1996) address the details of the streamline topology near the jet nozzle. Measurements of the velocity field in the symmetry plane have also been described in several previous studies (Patrick 1967; Chassaing *et al.* 1974; Andreopoulos & Rode 1985; Kelso *et al.* 1996; Gogineni, Goss & Roquemore 1995). However, only the results of Patrick (1967) present detailed velocity fields for $r > 8$. The present work complements these data by providing symmetry-plane data for $r = 10$ and $r = 21$. Investigation of the streamline topology in the near field of transverse jets issuing from a pipe, will also be compared with the results of Kelso *et al.* (1996).

(*b*) Further assessment of the assumption of intermediate-asymptotic similarity in strong transverse jets. This assumption was the cornerstone of the analytical work presented in Part 1. Jet trajectories, and velocity along these trajectories, will be compared with predictions. Furthermore, mean velocity and RMS fluctuation profiles will be shown to collapse in the similarity coordinates suggested by Part 1 of this paper.

† Present address: Department of Mechanical Engineering, University of Michigan, Ann Arbor, MI 48109-2121, USA.

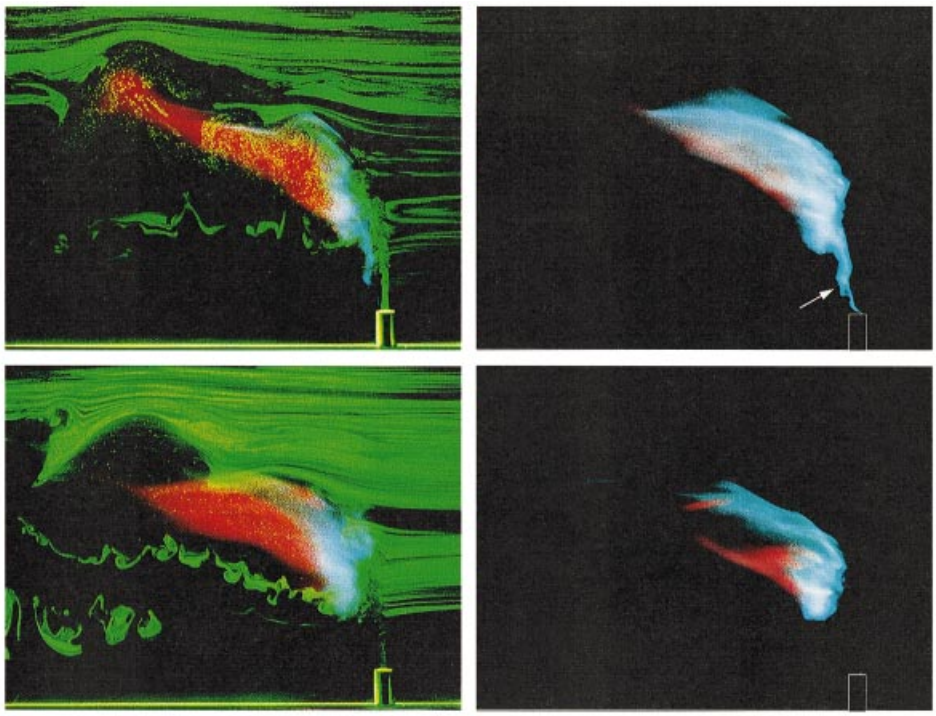

FIGURE 2. For caption see facing page.

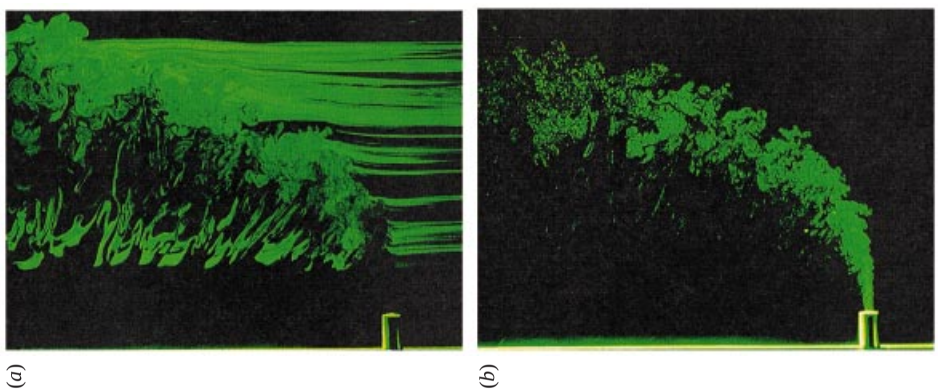

FIGURE 1. For caption see facing page.

(*c*) Evaluation of flow-field modification due to combustion heat release, specifically when the jet fluid is a gaseous hydrocarbon fuel. This investigation is motivated by the results of Gollahalli, Brzustowski & Sullivan (1975), who studied a non-buoyant high Reynolds number propane diffusion flame in a crossflow. The trajectories they measured are close enough to non-reacting jet results that it seemed possible to extend the analysis in Part 1 to burning jets, by using additional conservation laws. In particular, we had hoped that the flame could be accounted for by assuming that it enveloped the jet, and resided away from the turbulent core of the jet, as suggested by several imaging studies of piloted free and co-flowing jet flames. In this case the effect of the flame would primarily be to reduce the crossflow density before it is entrained into the jet. However, in this paper we show that flame liftoff, due to the interplay between turbulence and finite-rate chemistry, complicates the situation. We also present a qualitative evaluation of turbulence/chemistry interactions in the flame by comparing velocity and OH radical concentration fields.

As an introduction to the particular jets and flames studied here, we present flow visualization images in figures 1 and 2. In figure 1, a pulsed sheet of laser light from a Nd : YAG laser illuminates glycerol fog particles seeded into the crossflow (*a*) or alumina particles seeded into the jet (*b*). The crossflow-seeded photo shows that the turbulent scales in the wake behind the jet are significantly more laminar than the turbulence within the jet. The jet exit Reynolds number is 3600, and so we expect turbulent flow in the jet. However, the Reynolds number based on crossflow velocity is only 400; thus larger-scale stirring motions are observed in the wake.

Figure 1 also demonstrates a phenomenon discussed in detail by Smith & Mungal (1998) and Fric & Roshko (1994): jet fluid is deposited into the wake, and vice versa. A practical implication of this observation is that the wake behind a fuel jet may contain flammable concentrations of fuel. Another practical implication of this behaviour is that waste gases issuing from a flare stack may escape into the wake, if the flame is lifted.

Interestingly, keeping a flame attached to the nozzle of a transverse jets is not trivial. In fact, keeping the flame completely attached has not proven to be possible at the scale of the present experiments, as shown in figure 2. The four images are of a transverse methane jet flame at the same conditions as the cold jet in figure 1. The top images are obtained by averaging flame emission over 1/30 s exposure time, using ASA 1600 film, during which a single pulse from the laser provides a practically instantaneous image of the Mie scattering from the particles seeded into the flow. On the left, (*a*), is an unpiloted pure methane jet; on the right, (*b*), a coannular hydrogen pilot ignites the methane jet. A comparison of the two flames' emission without the laser illumination is shown on the bottom row. The pilot ignites only a thin sliver of methane on the lee side of the jet, indicated by the arrow. The main body of the flame still appears lifted, and the jet entrains and mixes significant amounts of air with fuel before the main flame base is reached. Because the pilot does not ignite a flame which

FIGURE 1. Flow visualization photographs of a transverse jet, $r = 8.9$, $Re = 3633$. Laser sheet illumination of alumina particles seeded into the jet (*a*), and glycerol fog seeded into the crossflow (*b*). Note that the ID of the nozzle is about half the OD; see figure 5 for jet exit detail.

FIGURE 2. Photographs of a transverse jet flame, $r = 8.9$, $Re = 3633$: (*a*) unpiloted flame; (*b*) piloted flame. Unpiloted flames are used for all measurements that follow. Top row photographs are obtained with crossflow fog illuminated by Nd : YAG laser sheet. Bottom row photographs have approximate outline of jet nozzle superimposed. Arrow in bottom right photograph points to the pilot flame, as distinguished from main flame body.

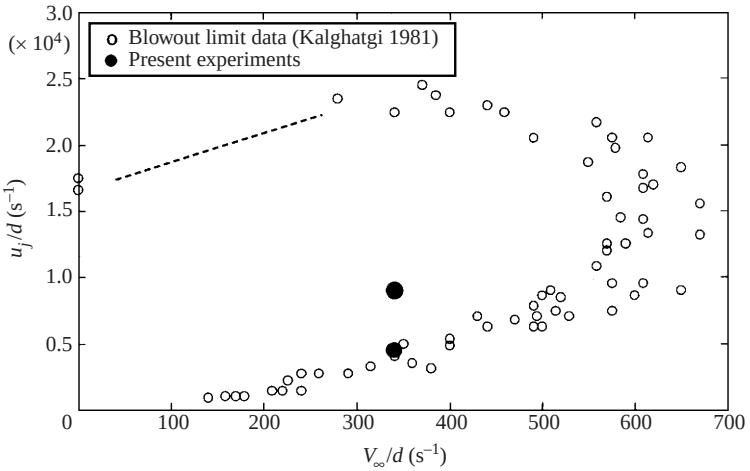

FIGURE 3. Experimental conditions for $r = 10$ and $r = 21$ flame cases, compared with blowout limits for transverse jets (from Kalghatgi 1981). For conditions outside the envelope of data points, the flames blow out.

surrounds the entire jet, the pilot complicates the flow, rather than simplifying it. For this reason, the unpiloted case was selected for detailed velocity field measurements.

2. Experiment

The scope of the present experiments is to compare jets at two blowing ratios, $r = 10$ and $r = 21$, in both non-reacting and burning (unpiloted) cases. These cases were chosen for comparison to the work of Smith (1996) and Smith & Mungal (1998). The selection also reflects their observation that when $r \geqslant 10$, the jet is not strongly influenced by the presence of the wall. In all cases, the jet was composed of 99.0% methane.

To prevent significant wind tunnel confinement effects, the jet diameter was chosen to be less than 0.5 cm so that the outer length scale of the jet, rd, did not exceed 10 cm, or $1/5$ the wind tunnel width. Flame stability considerations then determined the crossflow velocity, which was chosen to achieve the highest possible Reynolds number, yet support a stable flame. The $r = 10$ and $r = 21$ cases are shown compared to flame blowout limits (Kalghatgi 1981) in figure 3. The $r = 10$ flame ($Re = 6300$) is very near the lower blowout limit, which limits the wind tunnel speed for this case to 1.6 m s^{-1}. This, in turn, limits the maximum Reynolds number to 6300 and 12 600 for the two cases.

The velocity field in the symmetry (x, y)-plane of each jet and flame is obtained using particle image velocimetry (PIV). In the flame cases, simultaneous planar laser-induced fluorescence (PLIF) imaging of the OH radical and PIV are also performed at five key locations in order to investigate the interaction between combustion reaction and turbulent flow. Further details and experimental considerations are given below.

2.1. *Wind tunnel, jet tube, and particle seeding systems*

The flow facility, shown schematically in figure 4, is a low-speed indraught aluminium wind tunnel used in a previous investigation (Smith & Mungal 1998), with minor improvements. The tunnel has a 50×50 cm cross-section and rounded inlet with 2.5 : 1 contraction ratio. For optical access, it has a large $50 \times 80 \times 0.63$ cm Pyrex

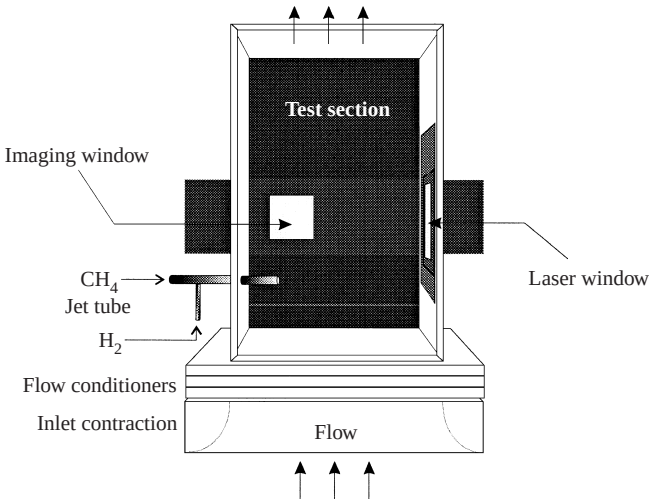

FIGURE 4. Wind tunnel schematic.

window on one side, a $15 \times 15 \times 0.95$ cm quartz window on the opposite side, and a $5 \times 25 \times 0.4$ cm quartz window on the wall opposite the jet exit for laser access. The quartz windows (Esco Products, Inc., S1-UV grade) are mounted in one of several plates, which can be rearranged to afford optical access throughout the tunnel section, and which in conjunction form a portion of the tunnel wall. The interior of the wind tunnel is painted black to reduce reflections. The inlet flow is conditioned by two 3 mm cell honeycomb sections, 1.25 cm and 2.5 cm thick, followed by a cascade of four screens, the last of which is a 12 wires-per-cm fine screen.

Maximum tunnel speed is approximately $10\,\mathrm{m\,s^{-1}}$. However, a methane flame cannot be sustained in the tunnel at this wind speed, so about 2/3 overfire air is drawn from the mezzanine above the laboratory to reduce the maximum tunnel speed to $3.0\,\mathrm{m\,s^{-1}}$. This also has the benefit of reducing the temperature of the combustion products before they reach the blower. Fine control of wind tunnel speed is attained by proportioning the air flow through the tunnel and a bypass inlet located in the ceiling of the laboratory. The wind tunnel test section has a mean velocity profile with less than 5% maximum-to-minimum variation, as measured using both PIV and hot-wire anemometry (Hasselbrink 1999; Smith 1996). Free-stream turbulence is approximately 0.8% across the tunnel span, with a slight increase near the jet nozzle, where the turbulence intensity rises to 1%.

Methane (Praxair, 99.0% Commercial grade) is delivered from cylinders, metered by a regulator to about 1 atm gauge pressure and delivered to a flow control panel. Flow rate is monitored using a glass tube flowmeter with a stainless-steel float (Matheson 605), and a pressure gauge (Norgren, 0–2 atm range). At the panel, methane is directed to a particle seeder/cyclone system, which is described below in greater detail. The methane is then directed to the jet tube via several metres length of stainless steel 9.5 mm tubing. Conductive tubing is required post-seeder, to prevent the development of high streaming potentials. Impolene tubing was used in a preliminary experiment, resulting in dangerous, but spectacular, electrical discharges between the seeder and cyclone.

The methane jet is injected normal to the crossflow through a 25 cm long tube (6.35 mm OD, 4.72 mm ID, 316 stainless steel), protruding 7 cm into the wind tunnel.

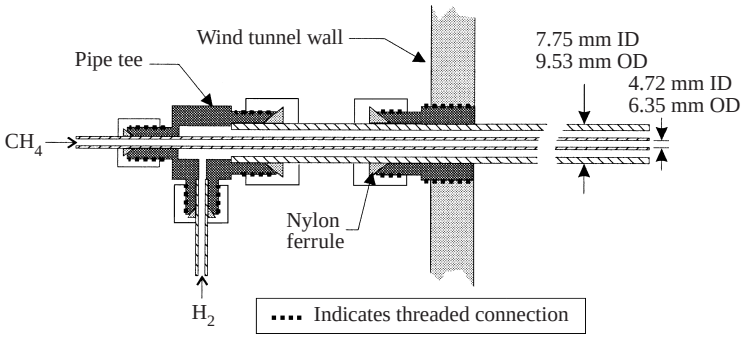

FIGURE 5. Jet tube detail. A standard run tee is been modified to allow the jet tube to pass through; other tube connections to the tee are standard. Note the coannular tube for the hydrogen pilot.

As shown in figure 5, the jet tube is located within an annular tube (9.5 mm OD) which can be used as a hydrogen pilot.

In all experiments the jet is seeded with 0.3 μm (nominal) alumina (Al_2O_3) particles, using a stirred fluidized-bed seeder and a conical cyclone to remove large agglomerates of particles. The seeder design is based on published design rules (Cheremisinoff & Cheremisinoff 1984; Nichols 1985; Ross 1993). Unseeded air is piped into the seeder through 9.5 mm copper tube. The last 10 cm of the tube, which encircles the bottom of the seeder, has small holes drilled along its axis, and the end of the tube is sealed. A rod fitted with a steel impeller is introduced through the top of the seeder, which allows stirring of the particles to maintain the fluidized state of the particle bed. Seeded methane is sent directly to the jet tube.

In reacting experiments, an identical seeder/cyclone system delivers seeded air for the crossflow via a jet-ejector channel. The air is fed to two 9 mm tubes which issue as turbulent jets into a 50 cm long rectangular channel (25 × 16 cm), capped with an aluminium honeycomb. A small fan at the channel entrance is used to overcome the losses associated with the honeycomb at the end of the jet-ejector pipe. This system satisfies requirements for both uniform particle density and low turbulence, by first exploiting turbulent mixing of the jets and entrained air in the confined channel, and then straightening the flow with a honeycomb section. In terms of maximum achievable seeding density and low wind tunnel turbulence, this arrangement was found to be superior to using several small-diameter jets issuing into open air underneath the tunnel. In non-reacting experiments, the crossflow is seeded with glycerol fog supplied by a theatrical fog generator (Rosco Model 1500). The fog issues through plastic pipe fittings arranged into two jets, which also issue into the entrance of the jet-ejector channel.

2.2. *Flow conditions*

2.2.1. *Blowing ratio and Reynolds number*

Transverse jet behaviour depends largely on two parameters: the jet-exit Reynolds number, Re and the blowing ratio, r. Table 1 summarizes these values for the cases studied, using the nominal value of $\bar{v}_\infty = 157.5\,\mathrm{cm\,s^{-1}}$ in the calculation of r. The table also summarizes the uncertainty in r, and the spatial variances in the v_∞ profiles.

The definition of r is an important subtlety. Blowing ratio is popularly defined as $r = (\rho_j u_j^2/\rho_\infty v_\infty^2)^{1/2}$, where subscript j denotes properties at the jet nozzle and subscript ∞ denotes those in the undisturbed crossflow, but since velocity profiles are not perfectly uniform, the definitions of v_∞ and u_j leave room for ambiguity. In the

	Case			
Parameter	$r = 10$ jet	$r = 10$ flame	$r = 21$ jet	$r = 21$ flame
r	$10.0 \pm 2\%$	$10.0 \pm 2\%$	$21.4 \pm 3\%$	$21.4 \pm 3\%$
u_j (m s^{-1})	21.3	21.3	45.5	45.5
Re	6000	6000	12 800	12 800
$\bar{v}_\infty$ measured (cm s^{-1})	156.8	158.5	157.0	158.0
RMS v_∞ (%)	1.1	1.5	2.7	1.7
v_∞ nominal (cm s^{-1})	157.5	157.5	157.5	157.5
Flame length L_f (m)	—	0.21	—	0.28
L_f/d	—	59	—	64
L_f/d^*	—	79	—	86
Richardson number, Ri	—	9.9×10^{-5}	—	2.2×10^{-5}
$Ri^{1/3}$	—	0.046	—	0.028
$\xi_L = Ri^{1/3} L_f/d$	—	2.7	—	1.8
Momentum length L_{mom}/d	—	32	—	54

TABLE 1. Run conditions. RMS v_∞ is a spatial RMS taken over the $v_\infty(x)$ profile. $d^* = (\rho_j/\rho_\infty)^{1/2} d$ is the momentum diameter of the jet.

present work we define r based on the profile-average cross-stream velocity, v_∞, and on u_j defined by the momentum flux:

$$u_j \equiv (J/\rho_j A_j)^{1/2}, \tag{2.1}$$

where

$$J = \lim_{T\to\infty} \frac{1}{T} \int_0^T \int_A \rho_j u^2 \, \mathrm{d}A \, \mathrm{d}t, \tag{2.2}$$

and A denotes the area of the jet exit, and t denotes time. Thus u_j is the equivalent uniform jet-exit velocity with the same momentum flux. J is calculated for each case from 100 instantaneous PIV measurements of jet exit velocity profiles, including the contribution due to RMS fluctuations obtained by Reynolds' decomposition. Values for r and Re are defined as

$$r \equiv \left(\frac{\rho_j u_j^2}{\rho_\infty \overline{v_\infty}^2} \right)^{1/2} = \left(\frac{J}{\rho_\infty \overline{v_\infty}^2 A} \right)^{1/2}, \tag{2.3}$$

$$Re \equiv \frac{u_j d}{\nu} = \left(\frac{J}{\rho_j A} \right)^{1/2} \frac{d}{\nu}. \tag{2.4}$$

Further details are given in Hasselbrink (1999). Profiles of $u(y)$ and $u'_{rms}(y)$ near the jet exit are shown in figure 6.

2.2.2. *Estimation of buoyancy effects*

Berker & Yamazaki (1978) found that buoyancy in turbulent jet flames increases the entrainment rate and modifies the velocity profiles. They also note that it is difficult to reach conditions in the laboratory in which buoyancy has negligible effect over the entire flame. Defining a Richardson number $Ri = gd/u_j^2$, they found that buoyancy begins to affect the flow at a scaled distance along the jet axis, $\xi = Ri^{1/3} x/d \approx 1.5$. Buoyancy effects are moderate for $1.5 < \xi < 3$, and severe above this value. Their findings are based on experiments on free jet flames, however; transverse jet flames are

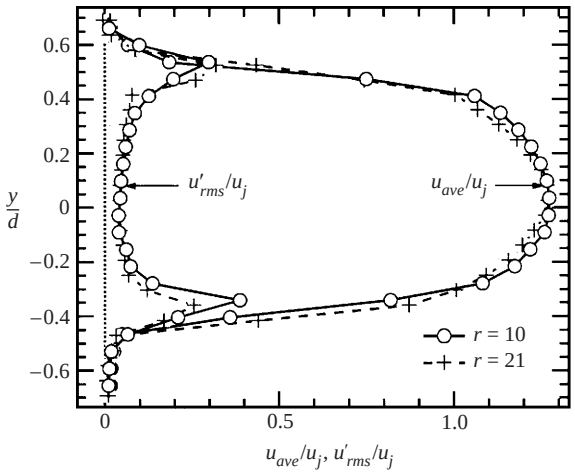

FIGURE 6. Mean and RMS velocity profiles near the jet exit. $r = 21$ case is taken at $x/d = 0.326$, $r = 10$ case is taken at $x/d = 0.413$.

expected to scale differently from free jets, and the buoyancy forces in our experiment are perpendicular to the jet momentum flux. Their findings are therefore used only as an estimate of the buoyancy magnitude.

Table 1 lists values for the flame lengths, Richardson numbers, and ξ_L (ξ at the end of the flame) for the two jet flames studied here. The tabulated flame lengths are the chord length from the flame base to the visible flame tip. For the $r = 10$ case, $\xi_L = 2.7$, indicating that buoyancy effects are moderate to strong at the flame tip. For the $r = 21$ case, $\xi_L = 1.8$, suggesting that the $r = 21$ flame is only slightly affected by buoyancy. Table 1 also lists the distance along the flame at which $\xi = 1.5$; this is called L_{mom}/d, the 'momentum length' of the flame, i.e. the length over which momentum dominates over buoyancy.

2.3. *OH PLIF imaging system*

2.3.1. *Excitation/detection strategy*

OH PLIF imaging is one of several possible techniques for detecting reaction zones in turbulent flames. Although high signal-to-noise OH PLIF imaging is possible using resonant excitation of OH with a tunable high-energy XeCl excimer light source (Seitzman & Hanson 1993), this excitation/collection scheme is not feasible simultaneously with PIV due to overwhelming elastic scattering by PIV tracer particles. Therefore the excitation/collection scheme in the present work is excitation of the $A^2\Sigma^+ \leftarrow X^2\Pi(1,0)$ band of OH near 283 nm, combined with detection of the (1,1) and (0,0) bands near 310 nm. Comparative advantages of this pumping scheme and spectroscopic details are given by Seitzman & Hanson (1993). OH absorption absolute linewidth (based on a Lorentzian lineshape) is approximately $0.04\,\mathrm{cm}^{-1}$ FWHM at 1800 K and atmospheric pressure; laser linewidth, however, is approximately $0.3\,\mathrm{cm}^{-1}$, implying that lineshape is unimportant and the assumption of a broad excitation source is valid. The $Q_1(6)$ transition is selected in order to minimize signal dependence on temperature (i.e. ground state population) and local composition. Barlow & Collignon (1991) have found that, although the quenching cross-section for OH fluorescence varies by about a factor of two across a typical flame, population fraction in the $Q_1(6)$ line varies oppositely, so that the signal should be proportional to OH concentration, to within 20% of peak OH concentration. An additional 15% uncertainty

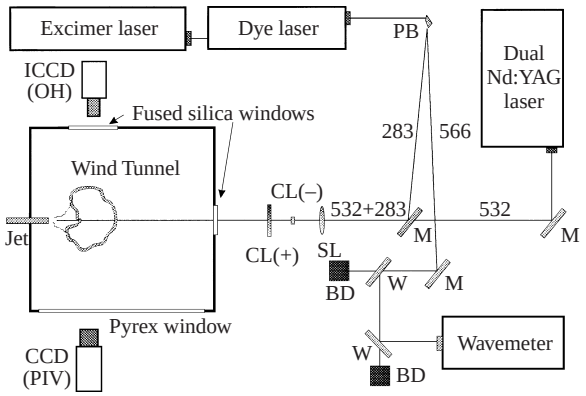

FIGURE 7. Experiment optical and electronics layout. M = mirror, W = window, SL = spherical lens, CL = cylindrical lens, PB = Pellin Brocca prism, BD = beam dump.

in this proportionality is introduced by laser sheet extinction as it propagates through a non-uniform density of particles before reaching the imaged region of the flow.

2.3.2. *Optical path*

Elements of the laser beam optical path are shown in figure 7. A Lambda-Physik EMG 230 XeCl excimer laser (308 nm, 300 mJ/pulse) pumps a grating-tuned Lambda-Physik FL-3002 dye laser using Coumarin 153 dye, providing 40 mJ/pulse at 566 nm. The beam is frequency-doubled to provide 3 mJ/pulse at 283 nm, then spatially separated from the fundamental beam with a single Pellin-Brocca prism. Approximately 8% of the fundamental is split off via an optical flat and directed to a pulsed wavemeter (Burleigh Instruments WA-4500) to assist in wavelength tuning. The frequency-doubled beam (about 3 mJ/pulse) is directed through turning mirrors and formed into a 250 μm thick × 45 mm tall sheet using a spherical lens ($f = 1$ m) and a 9 : 1 cylindrical telescope ($f = -25.4$ mm and $f = 250$ mm).

2.3.3. *OH image capture*

OH fluorescence is captured on a Princeton Instruments 512×512 Pentamax camera with a fibre-coupled MCP intensifier. The camera is equipped with a Nikkor f/4 UV lens, a Schott UG-11 filter to reject flame emission, and one Schott WG-305 filter (3 mm thick) to reject elastic scattering from the particles. The intensifier is gated to eliminate flame emission and any 532 nm scattering from the PIV laser pulses. The intensifier gate is opened approximately 60 ns before the laser pulse arrives in the test section, and is closed approximately 250 ns later.

The OH images are qualitative, intended only to visualize the location of flame zones. However, because the laser sheet intensity varies significantly across the viewing region, image corrections for the mean background and the mean laser sheet intensity profiles are applied. That is, the OH fluorescence signal F_{ij} at the pixel location (i, j) is calculated from the image intensity I_{ij} according to

$$F_{ij} = \frac{I_{ij} - \bar{B}}{\bar{L}_j - \bar{B}}. \tag{2.5}$$

Mean background $\bar{B}$ is calculated as the mean intensity of a camera image taken with no laser excitation. Mean laser sheet intensity distribution $\bar{L}_j$ was determined by imaging the vertical stripe of fluorescence created when the laser sheet illuminates a Schott

WG-305 filter placed at the image plane (Muller & Schefer 1997). The beam energy profile was determined by summing the intensity across horizontal rows in a neighbourhood around the fluorescence stripe. These profiles were averaged over 10 laser shots, and smoothed with a box-car filter, in order to provide the mean laser profile, $\bar{L}_j$.

We emphasize that the quantitative nature of the images is limited for several reasons. Most serious of these is that OH is a somewhat unreliable marker of heat release. It is produced by fast two-body reaction mechanisms but is consumed by slow three-body reactions; hence OH may exist in regions where the flow is hot, but overall reaction rate is quite slow. Recent work has demonstrated a more reliable, but more complicated method, using simultaneous CO/OH imaging. Therefore, no further steps are taken to attempt to interpret the OH images more quantitatively. Hasselbrink & Mungal (1998*b*) discuss (1) interpretation of the images, (2) rejection of elastic particle scattering, (3) the magnitude of laser-sheet extinction, and (4) the possibility of particle/flame interactions, in greater detail.

2.4. *PIV system*

2.4.1. *PIV hardware*

The PIV system hardware in this study, shown in figure 7, consists of:

a dual-cavity Nd : YAG laser (Spectra Physics PIV-400, 320 mJ/pulse at 532 nm, 15 Hz double-pulse repetition rate);

high reflectivity 532 nm dichroic mirrors (1 in. diameter) for beam steering, and sheet forming optics as described in § 2.3.2;

a high-resolution interline frame transfer CCD camera (1000 × 1000 9 μm pixel array, Kodak ES-1.0, 60% fill factor) with 105 mm Nikkor lens at f/5.6, mounted on a tilt/rotation stage (Newport Series 36);

a personal computer (200 MHz Pentium Pro, Micron Technologies) with a fast PCI frame grabber (provided by TSI, Inc.) to acquire and process the images;

digital delay generators (Stanford Research Systems DG-535) for laser, camera, and intensifier synchronization.

At times throughout this work, this laser and camera are called the 'PIV laser', and the 'PIV camera' as a shorthand, to distinguish them from their OH imaging counterparts.

2.4.2. *PIV image processing*

PIV image processing is performed with custom software, StanPIV, written as part of the present work. Detailed discussion of StanPIV is given by Hasselbrink (1999). The task of writing custom code was necessary because commercial PIV image processing code had a low probability of vector detection in regions where seeding density was low and displacement high. This is an unavoidable situation in flames, where density drops by a factor of about seven. StanPIV utilizes some of the more recently published advances in PIV image processing (Raffel, Willert & Kompenhans 1998) to achieve significantly higher probability of detection, as well as a factor of six reduction of systematic measurement bias error. The algorithm is based on the traditional two-frame FFT cross-correlation method. However, after the vector field is initially processed, filters are applied to the data to eliminate spurious vectors, and these vectors are linearly interpolated. Then the vector field is reprocessed, with the interrogation regions offset by the amount of the local particle displacement. In this way, the in-plane loss-of-correlation (Westerweel, Dabiri & Gharib 1997; Westerweel 1997) is minimized, and therefore the chance of valid vector detection is maximized.

Also, the interrogation region size may be reduced between iterations, providing greater resolution (at the cost of accuracy, of course). Up to eight iterations of this procedure are performed, at 3–4 times the computational expense of traditional PIV. However, data yield is better than 98.5% in the flame cases (99.5% in nonreacting cases), improved from less than 90% using commercial single-pass PIV with 32^2 interrogation windows. Average image processing time for 100×100 resolution (20-pixel final interrogation region size, 1000×1000 pixel images) is approximately one minute on a 400 MHz Intel Pentium II-based PC.

Once an ensemble of instantaneous vector fields has been obtained from a set of images, several post-processing calculations are made. Raw data are cast from pixel units into physical coordinates, and turbulence statistics and derived quantities such as vorticity and strain rate are calculated, again using custom software (Urban 1999).

2.4.3. *PIV uncertainty*

The accuracy of various image processing algorithms has been analysed in several papers (Ashforth-Frost *et al.* 1993; Westerweel 1993; Lourenco & Krothapalli 1995); a summary of their findings can be found in the recent book by Raffel *et al.* (1998). However, in flows with high temperature gradients, uncertainty is dominated by thermophoresis (Muñiz, Martinez & Mungal 1996), a phenomenon in which a particle experiences a force opposite to the direction of the fluid temperature gradient. Thermophoretic diffusivities have been measured directly by Gomez & Rosner (1993), and the effects of thermophoresis on velocity measurements in flames have been studied by Sung, Law & Axelbaum (1994), who also give formulae for the thermophoretic velocity (valid for particles smaller than 1 μm diameter). Thermophoretic velocities in flames are (worst-case: assuming $2000\,\mathrm{K\,mm^{-1}}$ temperature gradient at 1300 K, and using air properties) about $15\,\mathrm{cm\,s^{-1}}$. Although this may not be a large relative error in the measured velocity, it can introduce significant error for derivative quantities such as strain rates. The smallest grid spacing used in the present work is about 0.43 mm, which introduces a maximum uncertainty in central-difference first derivatives of about $240\,\mathrm{s^{-1}}$. This value is quite large compared to extinction strain rates for methane diffusion flames, which are on the order of $400\,\mathrm{s^{-1}}$. Uncertainty in vorticity, dilatation, and strain rates is larger by $\sqrt{2}$ because the calculation involves four velocity measurements for central differences. Hence the maximum uncertainty due to thermophoresis is approximately $340\,\mathrm{s^{-1}}$.

2.4.4. *Image registration*

In order that the data obtained from the OH camera and the PIV camera may be combined, it is necessary to transform the image pixels into a physical coordinate system. Before each experiment, each camera acquires an image of a ruled target printed at 600×600 dots-per-inch resolution on transparency film. In each image, two locations in the images are chosen as registration points, with physical coordinates (x_1, y_1) and (x_2, y_2), corresponding to pixel coordinates (i_1, j_1) and (i_2, j_2), respectively. In principle, four parameters can be determined by mapping these points to each other: magnification M, rotation, and offsets in the two Cartesian coordinate directions, b_x and b_y. However, it is found that fine-tuning the camera tilt with a micrometer tilt/rotation stage eliminates rotation to within the 1 pixel uncertainty of locating a vertex on the target. Therefore, instead of correcting for rotation, the transformation employed is a simple linear transformation

$$x = Mi + b_x, \tag{2.6}$$

$$y = Mj + b_y, \tag{2.7}$$

and the remaining three parameters M, b_x, and b_y are determined as the least-squares best fit. Since these are determined by two points, the least-squares best fit is the average of the value calculated using each registration point:

$$M = \frac{1}{2}\left(\frac{x_1 - x_2}{i_1 - i_2} + \frac{y_1 - y_2}{j_1 - j_2}\right), \tag{2.8}$$

$$b_x = \tfrac{1}{2}(x_1 - Mi_1 + x_2 - Mi_2), \tag{2.9}$$

$$b_y = \tfrac{1}{2}(y_1 - Mj_1 + y_2 - Mj_2). \tag{2.10}$$

The OH image is of significantly higher resolution (512×512) than the final PIV grid (100×100). Therefore, after coordinate transformation, software subsamples the OH image onto the PIV grid by averaging the OH signal in an $n \times n$ pixel neighbourhood nearest each PIV grid point, where n is the closest integer factor between PIV and OH image resolutions. In the present experiments $n = 5$, such that the final resolution of the OH image is 0.3 mm. However, the shortest length scale of OH we expect to find in a turbulent flame is $(D_{OH}/S_{ext})^{1/2} = 0.3\,\text{mm}$, where the mass diffusivity of OH is $D_{OH} \approx 1.5 \times 10^{-4}\,\text{m}\,\text{s}^{-1}$ and the flame extinction strain rate is $S_{ext} = 1772\,\text{s}^{-1}$ (Law, Zhu & Yu 1986).

2.5. *Imaging locations and resolution*

There are several important length scales in the transverse jet flow: the outer length scale, rd, over which the jet deflection occurs; the near-field length scale d, over which the jet-like region scales; and turbulence length scales, the smallest of which is the Kolmogorov scale η_K. Unfortunately, the dynamic range of these scales is at least two orders of magnitude greater than the PIV grid. In order to prevent spatial smearing of the results, our approach has been to image small subregions of the flow, and assemble these results into a mosaic of the larger-scale flow.

The largest length scales are $rd = 4.6\,\text{cm}$ and 9.2 cm, for the two cases studied here. The smallest viscous scale, η_v, is proportional to the Kolmogorov scale,

$$\eta_v = c_v \eta_K = c_v \delta Re_\delta^{-3/4}, \tag{2.11}$$

where the constant c_v is not agreed upon, but for the sake of estimation, we take it to be $O(10)$ based on previous experiments (Dowling & Dimotakis 1990; Buch & Dahm 1998). The smallest length scale is therefore 1/100 the local jet width. At the end of the potential core, taking $\delta = d = 0.46\,\text{cm}$, we have $\eta_v = 46\,\mu\text{m}$, which is virtually impossible to resolve with PIV in a gas-phase flow.

Fortunately, the turbulence statistics u'_{rms} and v'_{rms} are largely determined by the large-scale motions of the flow. It is possible to estimate the relative measurement error in these quantities due to the filtering represented by the interrogation region (IR). Assuming that the energy spectrum has a $-5/3$ power-law dependence on the wavenumber, and that the IR represents a top-hat filter in wavenumber space, the fluctuation energy measured is approximately

$$\frac{E_{meas}}{E_{total}} \approx \frac{\displaystyle\int_{1/\delta}^{1/2\lambda_m} k^{-5/3}\,\mathrm{d}k}{\displaystyle\int_{1/\delta}^{1/\eta_v} k^{-5/3}\,\mathrm{d}k} = \frac{1 - (2\lambda_m/\delta)^{2/3}}{1 - c_v^{2/3} Re^{-1/2}}. \tag{2.12}$$

As a compromise between measurement accuracy and practicality, the present experiments keep $\lambda_m/\delta \leqslant 1/20$. Hence we can expect to capture about 83% of the

	Full-field PIV expts		
	Near field	Far field	Simultaneous PIV/OH expts
Image size	1008×1016	1008×1016	1008×1016
Vector grid	64×64	64×100	64×64
Magnification ($\mathrm{px\,mm^{-1}}$)	37.08	18.93	34.4
Interrogation region (px)	32	32	32
Grid spacing (mm)	0.431	0.845	0.465

TABLE 2. PIV imaging parameters.

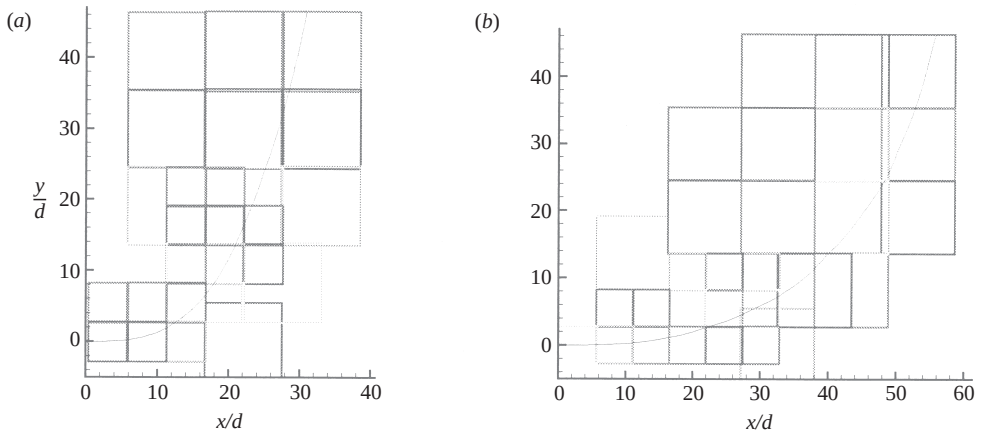

FIGURE 8. PIV image windows: (*a*) $r = 10$ jet, (*b*) $r = 21$ jet. Squares are edges of PIV imaging region tiles, which form a mosaic of the flow. Each tile represents a 64×64 grid of velocity vectors. The centreline streamtrace for each jet is shown for reference.

fluctuation energy, i.e. the measured value of u'_{rms} should be about 91% of the true value.

Since the jet width increases downstream, two sizes of imaging windows have been used for the PIV imaging experiments. The high-resolution window, used in the near field, is approximately 2.5 cm square, while the low-resolution window used elsewhere is approximately twice this size. Typical imaging regions are shown in figure 8. Each square represents one imaging region of 64×64 gridpoints. The jet trajectory is shown as a reference; resolution of the grid is kept highest along the jet centreline, and jumps to low resolution once $x/d > 28$ cm ($\delta \approx 5.5$ cm). The only region of the flow in which $\lambda_m/\delta > 1/20$ is in the first imaging region at the nozzle, which represents the first six diameters of the jet trajectory. Unfortunately, PIV measurement resolution in this region was limited by achievable particle density.

Image acquisition and processing parameters are given in table 2. Typical interrogation region size (final pass) is 32 pixels. The resolution in physical space depends on the magnification used, but typically this is either 37 pixels $\mathrm{mm^{-1}}$ or 19 pixels $\mathrm{mm^{-1}}$ for the cases studied in the present work. Approximately 110 vector fields are obtained at each window, and statistics are calculated from these data. Convergence tests suggest that the mean values are converged to within 3%, and RMS u' and v' are converged to within 7%.

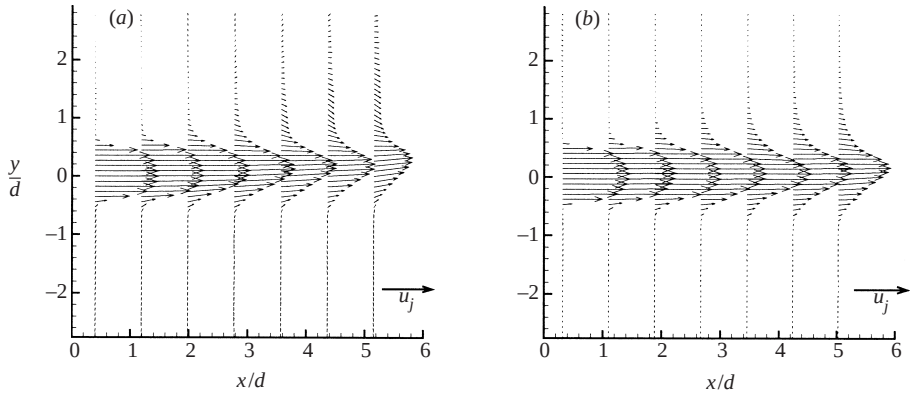

FIGURE 9. Average velocity profiles in the potential core region. (*a*) $r = 10$ non-reacting jet; (*b*) $r = 21$ non-reacting jet. Flame cases are similar due to lack of flame at jet exit (see figure 2).

3. Results: flow structure

3.1. *Near-field flow structure*

Figure 9 shows ensemble-averaged velocity profiles in the potential core region of the $r = 10$ and the $r = 21$ jets. The differences from average profiles observed for free jets are subtle, and are more pronounced in the $r = 10$ jet: by $x/d = 5$, the velocity profile is skewed towards the lee side, and the u velocity does not decay to zero rapidly on the lee side. The profiles for $r = 21$, however, appear much more like those of a free jet, as might be expected.

A reference vector of length u_j is shown in these figures; we note that the peak values of $\bar{u}$ observed in the profiles exceeds u_j by approximately 20%. Since u_j is defined as the velocity of a uniform jet exit velocity profile with the same momentum flux, the peak velocity is expected to be somewhat higher than u_j due to the boundary layers in the pipe. A similar 20% 'overshoot' was also reported by Becker & Yamazaki (1978).

A sample of four instantaneous vector fields in the potential core region is shown in figure 10. The arrowhead density reveals a behaviour often noted in free turbulent jets: shear planes tend to align themselves at 45° to the jet axis. However, streamtraces, integrated from the velocity field, highlight the asymmetry, and reveal vortical 'sinks' (in two dimensions) on the windward side, as well as a persistent 'source' on the lee side of the jet. In contrast, free and coflowing jet flow fields have no points in the instantaneous flow where velocity magnitude is zero, in the lab frame of reference (Muñiz 2001).

Figure 11(*a*) shows streamtraces in the near field, overlaying colour contours of the two-dimensional divergence, defined as

$$\nabla_{2D} \cdot \boldsymbol{u} = \frac{\partial u}{\partial x} + \frac{\partial v}{\partial y}. \tag{3.1}$$

This quantity is calculated using central differences from the velocity data. The lee-side source observed in the instantaneous field is a dominant feature of the near-field symmetry plane; in fact, in this plane, all time-averaged flow on the lee side of the jet is apparently sourced from this node. The existence of this node was also found by Kelso *et al.* (1996) for lower-r jets, using a flying-hot-wire technique, and by Sykes, Lewellen & Parker (1986), in a computational study. In both of these studies, the jet

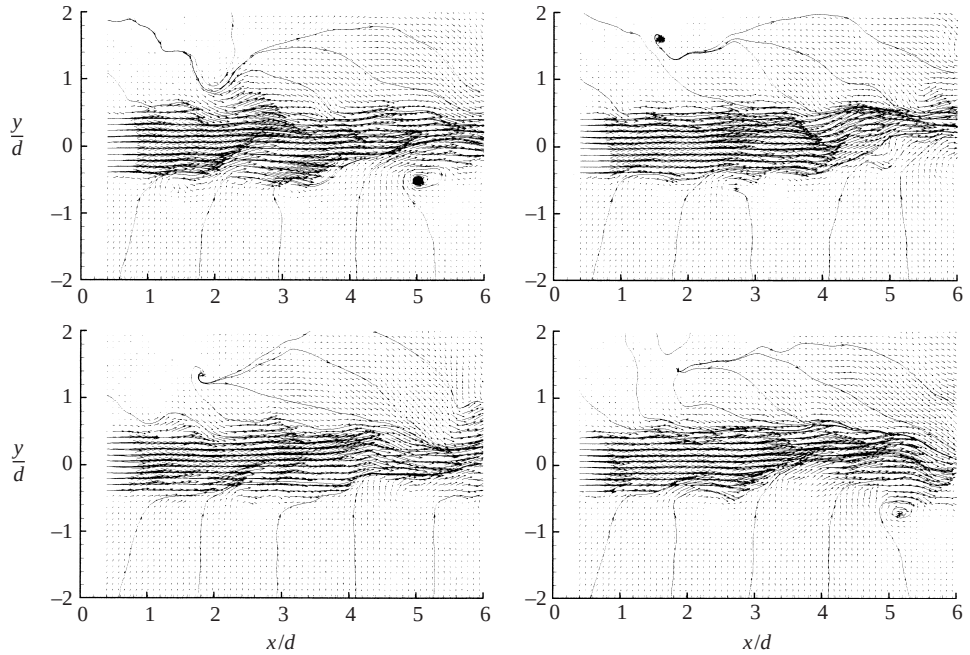

FIGURE 10. Four samples of instantaneous velocity fields in the potential core region. All cases are the $r = 10$ non-reacting jet. Flame cases are similar due to lack of flame at jet exit (see figure. 2).

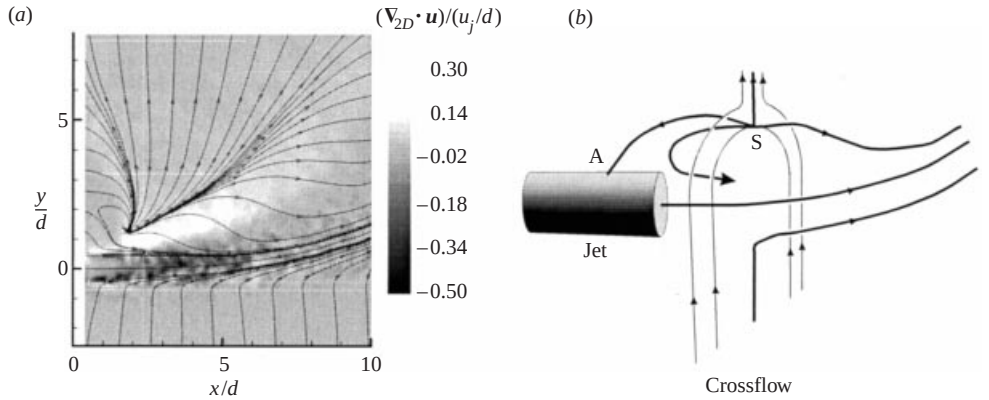

FIGURE 11. (*a*) Two-dimensional divergence, overlaid with two-dimensional streamtraces, in the near field. Streamtraces are everywhere parallel to the measured two-dimensional velocity field, but are not contours of constant streamfunction. (*b*) Interpretation of three-dimensional near-field streamlines. Area of high two-dimensional divergence measured on lee side of the jet indicates highly compressive out-of-plane strain, implying opposing out-of-plane streamlines which meet at the stagnation point, S. However, the near-zero two-dimensional divergence on the windward side implies that streamlines do not diverge strongly out of plane on the windward side; instead, they are entrained into the jet.

issued from a wall. The results of Kelso *et al.* were of lower resolution than the present work, and the computation by Sykes *et al.* had a slip boundary condition at the wall; nonetheless, the present findings corroborate their discoveries, and demonstrate that the node exists without the presence of a wall boundary.

The out-of-plane flow pattern can be better understood by considering the out-of-

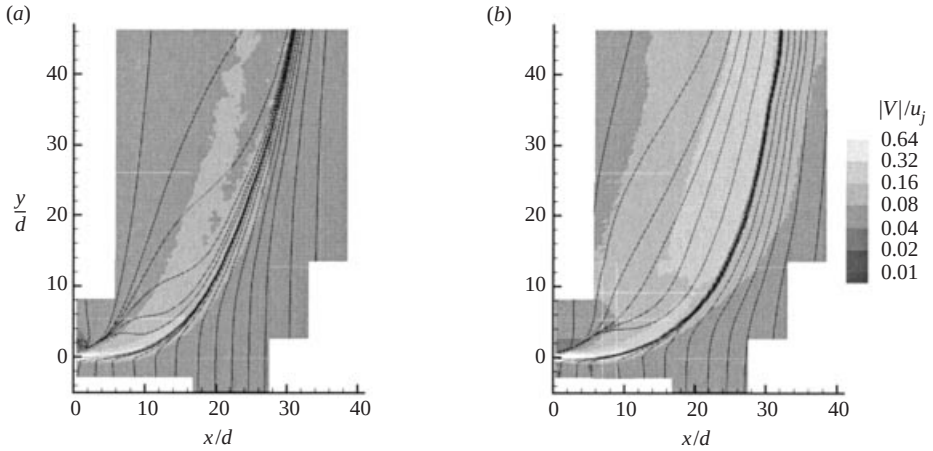

FIGURE 12. $r = 10$ streamtraces and velocity magnitude contours: (*a*) non-reacting jet; (*b*) methane flame.

plane extensional strain rate, $\partial w/\partial z$. Since the flame base is only present at the upper right corner of the $r = 10$ image, elsewhere the flow is divergence-free. Therefore the out-of-plane extensional strain rate is

$$\frac{\partial w}{\partial z} = -\nabla_{2D} \cdot \boldsymbol{u}. \tag{3.2}$$

From the in-plane streamline topology and $\nabla_{2D} \cdot \boldsymbol{u}$, it is possible to infer the out-of-plane streamline structure. Low values of $\nabla_{2D} \cdot \boldsymbol{u}$ in the jet result from the entrainment into the jet, and the out-of-plane growth of the jet. The high $\nabla_{2D} \cdot \boldsymbol{u}$ behind the jet suggests high compressive out-of-plane strains, i.e. $\partial w/\partial z$ has large negative values in this regions. Since $w = 0$ on the symmetry plane, this suggests opposed flow on the lee side, as illustrated in figure 11(*b*). The apparent lee-side source is labelled S. From this cartoon, it is also clear that another critical point must exist in the streamline pattern: a re-attachment point, labelled A, must exist somewhere on either the jet tube or the tunnel wall – its location in the cartoon was chosen arbitrarily. We note that a corresponding region of negative $\nabla_{2D} \cdot \boldsymbol{u}$ in front of the jet does not exist, suggesting that as crossflow fluid approaches the jet, it is entrained into the jet flow rather than passing around it. This underscores yet another important difference between transverse jets and cylinders in crossflow, as emphasized in numerous other ways by Fric & Roskho (1994) and others. It is suggested that this complex near-field flow deserves further investigation using a three-component (stereoscopic) PIV technique, in off-axis planes parallel to the symmetry plane.

3.2. *Far-field flow structure*

Greyscale maps of velocity magnitude, overlaid with streamtraces, are shown throughout the measured domain in figures 12 and 13 for each case. In these images, and those to follow, colour contours are shown using only 1/3 the resolution of the actual PIV vector grid, and the value at each point is shown as a square 'pixel' in order to prevent masking of the spatial resolution from the reader.

The non-reacting jets in figures 12 and 13 show some interesting features. First of all, in the near field, a very low-speed region is formed on the lee side, as might be expected. There is also a less pronounced low-speed region on the windward side of

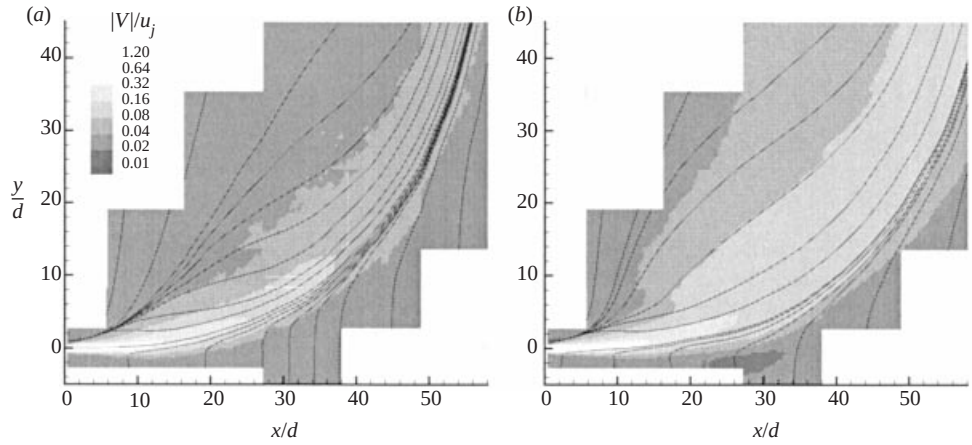

FIGURE 13. $r = 21$ streamtraces and velocity magnitude contours: (*a*) non-reacting jet; (*b*) methane flame.

the jet near $8 < x/d < 18$ for the $r = 10$ case, and near $17 < x/d < 46$ for the $r = 21$ case. This ensemble-averaged result is consistent with the observation of stagnation points in the instantaneous fields, presented in figure 10. It is somewhat surprising that crossflow streamtraces approaching the jet near the nozzle are deflected slightly towards the jet nozzle just before being entrained into the main jet flow. Presuming total pressure is conserved along these crossflow streamlines as they approach the jet (the crossflow is nearly irrotational), the speed reduction implies an increase in static pressure on the windward side of the jet. Hence the assumption that pressure drag plays no role in the jet deflection may be a very good approximation, but is probably not absolutely true.

The effect of igniting the methane jet is also shown in figures 12 and 13. The primary differences from the non-reacting case are: (1) higher post-flamebase velocity magnitude (about 2–3 times higher), (2) highly divergent streamlines on the lee side of the jet, and (3) a larger low-velocity region on the windward side of the jet. Further examination of the data will seek to quantify the increase of the velocity, and develop an explanation for the divergent streamlines on the lee side and the enlarged low-velocity region on the windward side.

Figures 14–17 each show greyscale maps of four normalized flow-field variables (left-to-right, then top-to-bottom): $\bar{u}/u_j$, $\bar{v}/v_\infty$, u'_{rms}/u_j and v'_{rms}/u_j. Each figure corresponds to one of the four cases; in order, they correspond to the $r = 10$ jet, the $r = 10$ flame, the $r = 21$ jet, and the $r = 21$ flame. The calculated jet-exit centreline streamtrace is shown in each figure for reference. In each case, some evidence of mismatch at the data window boundaries (figure 8) is evident. The causes contributing to this problem are: (1) fluctuations in the jet flow-rate setting, due to manual compensation for regulator drift from run to run, and (2) fluctuations in the wind tunnel velocity from run to run, caused by slight clogging of the wind tunnel screens by the alumina particles (flame cases only). We note that the worst mismatches usually occur in the far field, and in the flames. As expected, more noise is evident in the fluctuation data than in the averaged velocities; the fluctuation statistics are also much more sensitive to occasional spurious outliers.

Starting with the greyscale maps for the $r = 10$ jet (figure 14), the $\bar{u}$ contours (*a*) show the somewhat surprising result that the locus of points with maximum $\bar{u}$ in the

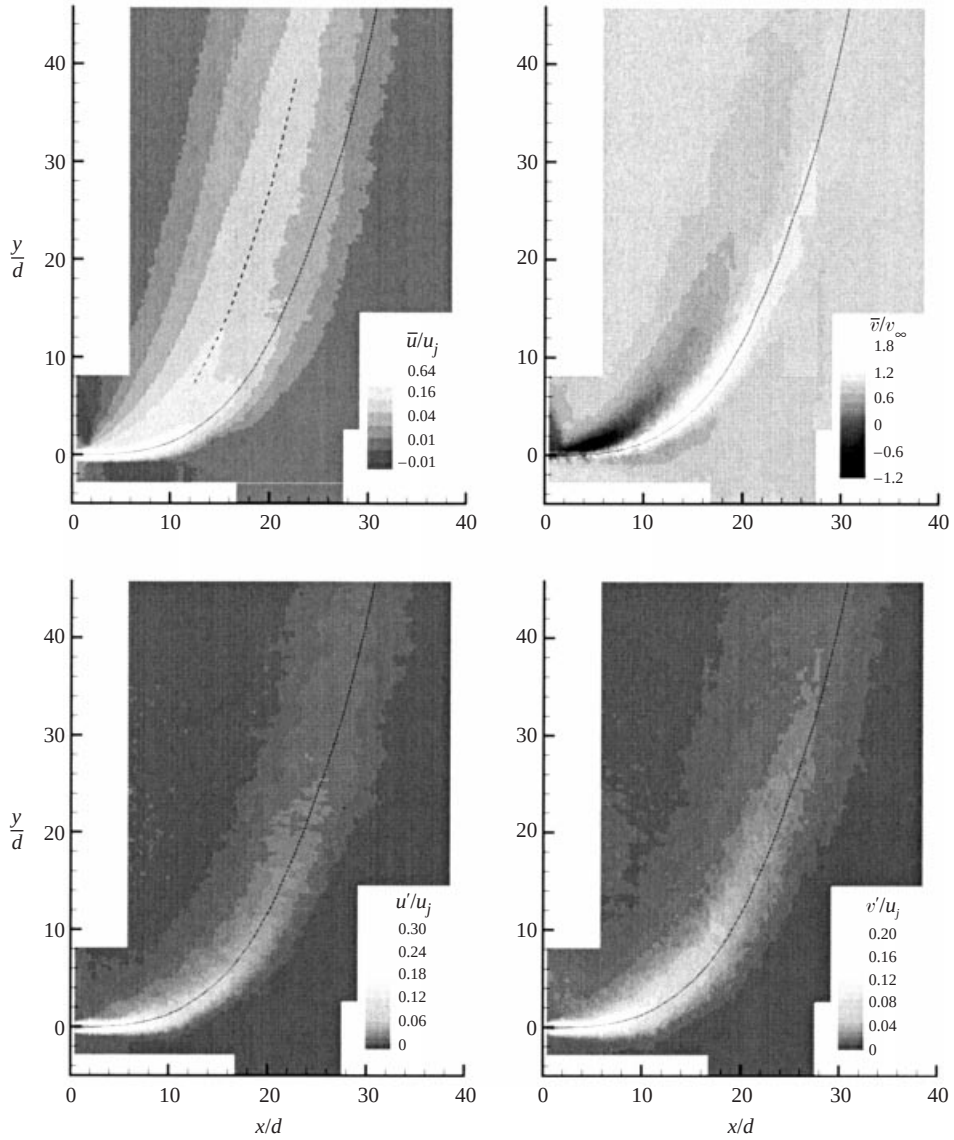

FIGURE 14. $r = 10$ non-reacting jet: greyscale maps of mean velocity components (top) and RMS velocity fluctuations (bottom). Quantities are labelled in individual legends. Contour levels of u, v, u' and v', span maximum to minimum values. Vorticity and divergence maps are reported in Hasselbrink (1999).

jet cross-section do not fall on the jet-centre streamline. Insofar as $\bar{u}/u_j$ is expected to behave similarly to a passive scalar issuing from the jet (as suggested by the analysis in Part 1), this behaviour is consistent with the finding by Kamotani & Greber (1972) that the passive scalar trajectory does not penetrate as far into the crosswind as the central streamline. Also, as profiles will demonstrate in § 4.1, the u profile in the region of rapid turning is doubly peaked. However, this is only faintly detectable in this greyscale map (even with strong look-up table biasing towards small u), owing to the large dynamic range in u displayed in this figure.

The map of $\bar{v}/v_\infty$ (b) shows that the $\bar{v}$ component of velocity can exceed the

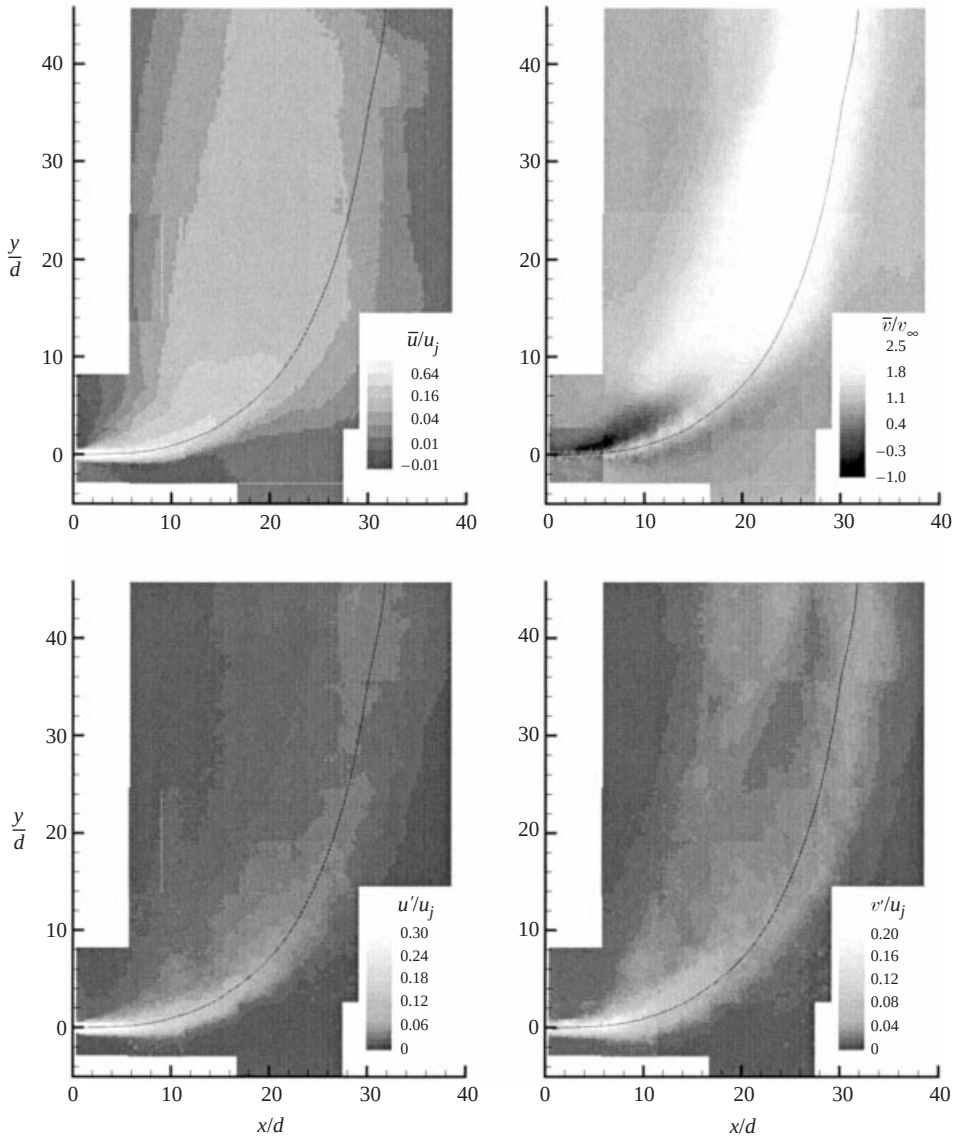

FIGURE 15. As figure 14 but for the $r = 10$ flame.

crossflow velocity, by a factor as large as about 1.8, and that this maximum value is usually found along the centre streamline. As noted in the $|V|$ contours, a thin region of reduced $\bar{v}$ is found along the windward edge of the jet; as the crossflow encounters the jet, it slows by about 40%. However, on the lee side, the effect of the jet on the v component is most pronounced: reverse flows with velocity of about $-1.2v_\infty$ can be found just behind the jet. The region of low $\bar{v}/v_\infty$ persists downstream; we note that the transition from green to yellow contours indicates $\bar{v}/v_\infty \approx 0.6$, and this contour extends downstream to $y/d = 16$.

RMS fluctuations are shown in parts (*b*) and (*c*) of greyscale maps. Once again the look-up table is strongly skewed towards small values in order to emphasize the structure of the flow field. The turbulence fluctuations are as high as $u'_{rms}/u_j = 0.3$,

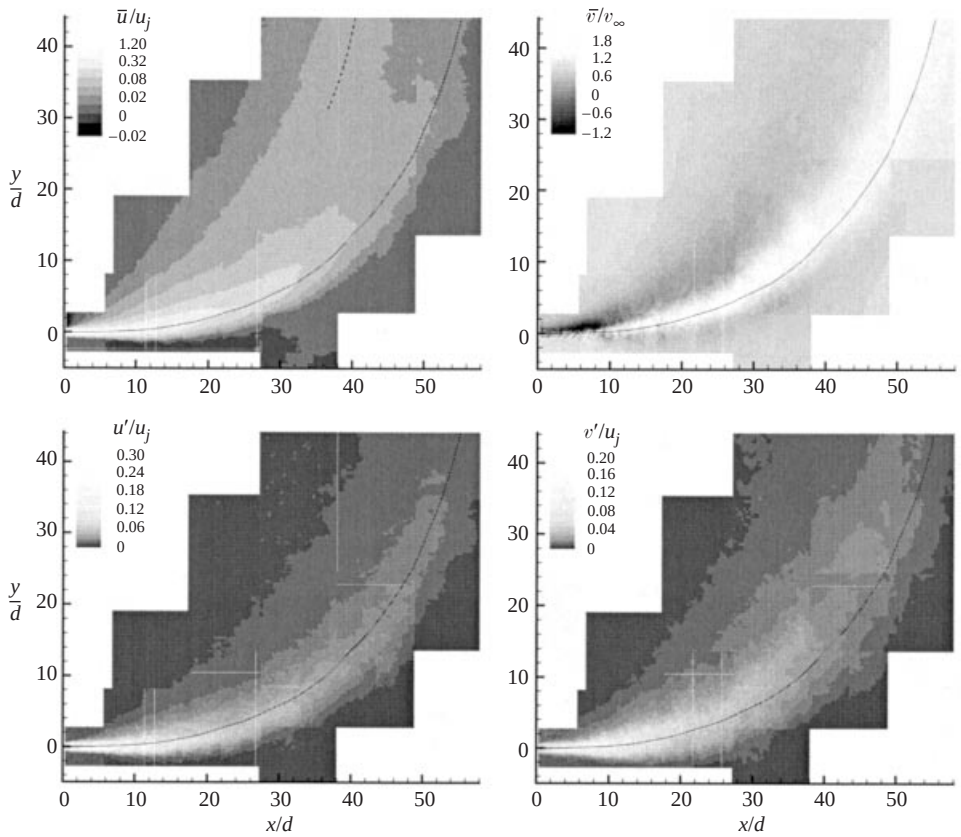

FIGURE 16. As figure 14 but for the $r = 21$ non-reacting jet.

and $v'_{rms}/u_j = 0.2$, with the largest values found (not surprisingly) in the jet shear layer. Unlike $\bar{u}$, the locus of u'_{rms} and v'_{rms} maxima correspond very closely to the location of the centre streamline.

The effects of igniting this methane jet are illustrated by the greyscale maps of figure 15. Not surprisingly, heat release increases both $\bar{u}$ and $\bar{v}$; perhaps somewhat surprising is the width of the region over which the $\bar{u}$ field is affected. The effect of heat release in the jet affects the surrounding flow significantly, over a distance which appears to scale with the size of the flame. Correspondingly, the $\bar{u}$ contours also become noticeably broader near $y/d = 10$; this will become more evident in the profiles to be presented in § 4.1.

The influence of heat release is perhaps most striking in the $\bar{v}$ greyscale map. Interestingly, the base of the flame outlined in this figure, and in the flow visualizations presented in figure 2, show that the flamebase is not orthogonal to the centre streamline; instead, it is nearly orthogonal to the crossflow. Furthermore, $\bar{v}/v_\infty \to 1$ no longer in the far field. With the flame, $\bar{v}/v_\infty \to 2.6$ at the flame tip. It is noted that this value is close to $(T_f/T_o)^{1/2}$, where T_f is the maximum flame temperature (probably very close to the adiabatic flame temperature of a stoichiometric methane/air flame, 2200 K), and T_o is the unburned gas temperature. This result suggests that the quantity ρv^2 is approximately conserved through the flame, as can be inferred from the Rankine–Hugoniot relations for a deflagration.

The flame appears to influence the structure of the v'_{rms} to a greater degree than

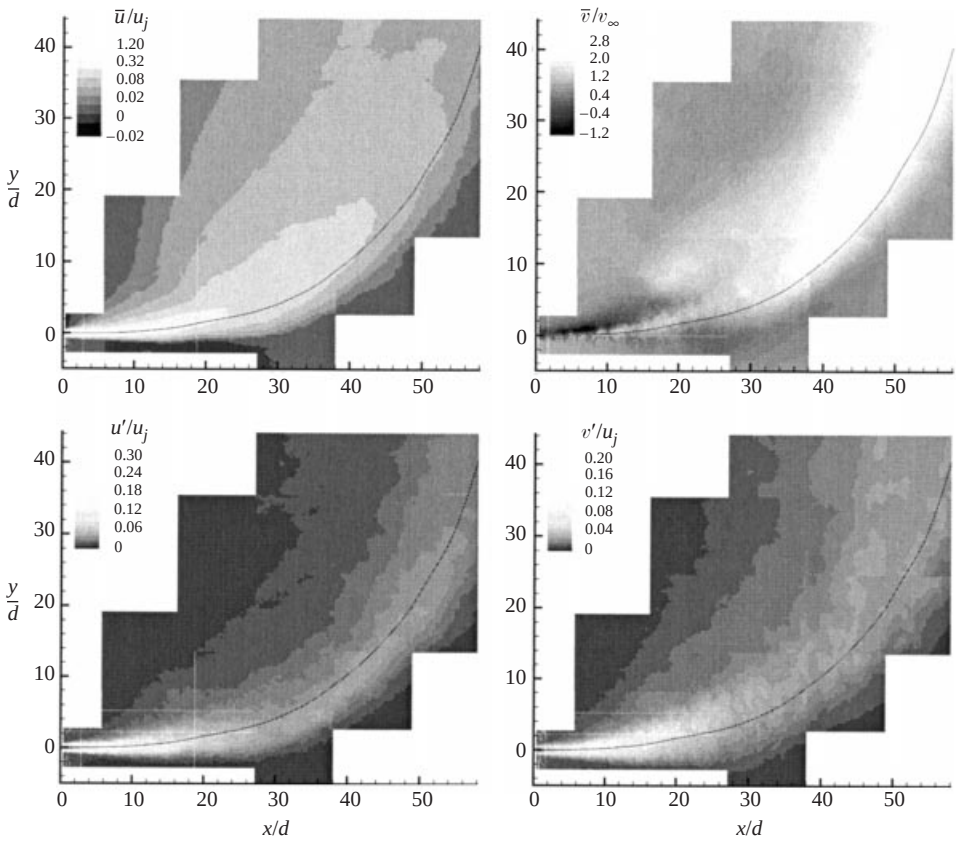

FIGURE 17. As figure 14 but for the $r = 21$ flame.

the u'_{rms} field. In particular, the contours of v'_{rms} appear to be highest in regions corresponding to the location of the flame envelope. We note that the bifurcation in the v'_{rms} contours does not become pronounced until near the end of the data window, suggesting that this may be a buoyancy effect. This possibility is supported by the previous estimate that buoyancy effects become important when $y/d \geqslant 33$ (§ 2.2).

We now turn our attention to figures 16 and 17 to explore the effect of increasing the blowing ratio. Since the outer length scale of the transverse jet flow is rd, the large-scale features of the $r = 21$ jet are about twice as large in the $(x/d, y/d)$ coordinate system. With this in mind, it is possible to check the scaling of various statistical properties with parameters such as u_j and v_∞, by comparing with the $r = 10$ case.

The $r = 21$ jet greyscale maps (figure 16) show very similar structure to the $r = 10$ jet. Furthermore, when the point-statistical properties are normalized, the maximum and minimum values observed in the $\bar{u}/u_j$, $\bar{v}/v_\infty$, u'_{rms}/u_j, and v'_{rms}/u_j fields (indicated as the maximum and minimum values on the look-up table) are very nearly equal for $r = 10$ and $r = 21$ cases.

Finally, the $r = 21$ flame (figure 17) shows a very similar flow field to the $r = 10$ flame. For this data set, the widening of the $\bar{u}$ contours is again obvious, as is the increase in $\bar{v}$, this time by a factor of 2.8, again very nearly $(T_f/T_o)^{1/2}$. Also note that the doubly peaked v'_{rms} contours observed in the $r = 10$ flame do not appear in the $r = 21$ flame. Since the $r = 21$ jet is less influenced by buoyancy, this again suggests that the doubly peaked $r = 10$ flame v'_{rms} contours are a result of buoyancy.

Quantity	Scaling law	Coefficient (Source)
Mass flux	$\frac{\dot{m}(x)}{\dot{m}_j} = c_{ej}\left(\frac{\rho_\infty}{\rho_j}\right)^{1/2}\left(\frac{x}{d}\right)$	$c_{ej} = 0.32$ (Ricou & Spalding 1961)
u velocity (jet direction)	$\frac{u_c}{u_j} = \frac{c_{un}}{c_{ej}}\left(\frac{\rho_j}{\rho_\infty}\right)^{1/2}\left(\frac{x}{d}\right)^{-1}$	$\frac{c_{un}}{c_{ej}} = 6.2$ (Chen & Rodi 1980)
v velocity (crossflow direction)	$\frac{v_\infty - v_c}{v_\infty} = \frac{c_{vn}}{c_{ej}}\left(\frac{\rho_j}{\rho_\infty}\right)^{1/2}\left(\frac{x}{d}\right)^{-1}$	$c_{vn} \approx 1.0$–2.0 (Calculated. 1.0 based on flat profile, 2.0 based on Gaussian deficit profile).
Scalar concentration	$\xi_c = \frac{c_\xi}{c_{ej}}\left(\frac{\rho_\infty}{\rho_j}\right)^{1/2}\left(\frac{x}{d}\right)^{-1}$	$\frac{c_\xi}{c_{ej}} = 5.0$ (Chen & Rodi 1980)
Trajectory	$\frac{x_c}{rd} = \left(\frac{2}{c_{ej}}\frac{y_c}{rd}\right)^{1/2}$	No data; see mass flux for estimate of c_{ej}.

TABLE 3. Jet-region ($x/d \gg 1$, $x/rd \ll 1$) scaling law summary.

4. Results: similarity

Part 1 of this paper assumed intermediate-asymptotic behaviour (Barenblatt 1996) in the transverse jet, and developed scaling laws for several flow-field variables in each of two regions: the near field, $x/rd \ll 1$, where the flow is jet-like, and the far field, $x/rd \gg 1$, where the flow is wake-like. These scaling laws are summarized in tables 3 and 4.

Experimental data from previous work were examined in Part 1 to confirm some of these results. The concentration data of Smith & Mungal (1998) confirmed that self-similar (jet-like) concentration profiles exist in the near field of high-r jets. It also confirmed that a relatively sharp transition from near-field to far-field scaling occurs near $x/rd = 0.75$ in jets with $r \geqslant 20$. Reasonable agreement with somewhat sparse centreline velocity data from the literature was presented as well. In this section, we confirm the existence of self-similar regions in the velocity field, in accordance with the scalings presented in table 3 and 4. We also present the effects of combustion heat release on the similarity.

4.1. *Mean velocity and fluctuation profiles*

The intermediate-asymptotic similarity theory presented in Part 1 predicts that the u-profiles are expected to collapse to a single curve when plotted in similarity coordinates:

$$\frac{u}{u_j}\frac{x}{d} = f\left(\frac{y}{x}\right). \tag{4.1}$$

It has also been shown in free jets that the RMS fluctuation u'_{rms} also collapses in these similarity coordinates (Champange 1978). Figure 18 shows these profiles for $r = 10$ and $r = 21$ jets (non-reacting). Collapse of the profiles is not observed in the $r = 10$ case, but this is not unexpected. As shown in Part 1, a jet-like region is only expected to appear in jets of $r > 20$, where $x/rd \ll 1$ and $x/d \gg 1$). The $r = 21$ velocity profiles at $x/d = 5$ and $x/d = 10$ collapse to the same curve, however. By $x/d = 20$, the requirement that $x/rd \gg 1$ has been exceeded, and collapse is not expected. These results are consistent with the extensive near-field concentration data presented in Part 1, which showed that concentration profiles begin to deviate from jet-similarity

Quantity	Scaling law	Coefficient (Source)
Mass flux	$\frac{\dot{m}(y)}{\dot{m}_j} = (9c_{ew})^{1/3} r \left(\frac{\rho_\infty}{\rho_j}\right)^{1/2} \left(\frac{y}{rd}\right)^{2/3}$	$c_{ew} = 0.32$–0.73 (Deduced from trajectories, tabulated below)
u velocity (jet direction)	$\frac{u_c}{u_j} = \frac{c_{uf}}{(9c_{ew})^{1/3}} \frac{1}{r} \left(\frac{\rho_j}{\rho_\infty}\right)^{1/2} \left(\frac{y}{rd}\right)^{-2/3}$	$c_{uf}/(9c_{ew})^{1/3} = 1.1$ (Present work. Data show u less than scaling law by up to a factor of 2. However, data are for centre streamline u, which is not the maximum u in cross-section.)
v velocity (crossflow direction)	$\frac{v_\infty - v_c}{v_\infty} = \frac{c_{vf}}{(9c_{ew})^{1/3}} \times \frac{1}{r} \left(\frac{\rho_j}{\rho_\infty}\right)^{1/2} \left(\frac{y}{rd}\right)^{-2/3}$	$c_{vf} \approx 2.0$ (Assuming Gaussian deficit profile)
Scalar concentration	$\xi_c = \frac{c_\xi}{(9c_{ew})^{1/3}} \frac{1}{r} \left(\frac{\rho_j}{\rho_\infty}\right)^{1/2} \left(\frac{y}{rd}\right)^{-2/3}$	$c_\xi/(9c_{ew})^{1/3} = 0.85$–$0.95$ (Data of Smith & Mungal (1998), see Part 1)
Trajectory (locus of maximum ξ; Section 3 shows that locus of maximum u also follows this trajectory)	$\frac{x_c}{rd} = \left(\frac{3}{c_{ew}} \frac{y_c}{rd}\right)^{1/3}$	$(3/c_{ew})^{1/3} = 1.6 \pm 0.2$ (Margason 1993; Margason 1968; Smith & Mungal 1998)
Jet-exit centre streamline trajectory	$\frac{x_c}{rd} = \left(\frac{3}{c_{ew}} \frac{y_c}{rd}\right)^{1/3}$	$(3/c_{ew})^{1/3} = 2.1$ (Present work)

TABLE 4. Wake-region ($x/rd \gg 1$) scaling law summary.

for $x/rd > 1/2$. In the far field, the v-velocity deficit (crossflow direction) is expected to be proportional to $(y/rd)^{-2/3}$, as shown in table 4. Given the trajectory in table 4, the intermediate-asymptotic similarity prediction is that (for $r \ll 1$, $x/rd > 1$)

$$r \left(\frac{v - v_\infty}{v_\infty}\right) \left(\frac{y}{rd}\right)^{2/3} = f\left(\frac{x/rd}{(y/rd)^{1/3}}\right). \tag{4.2}$$

Profiles of v and v'_{rms} in the non-reacting methane jets are plotted in these coordinates in figure 19. The $y/d = 10$ v-profiles for the $r = 10$ jet are outside the region of intermediate-asymptotic similarity. However, the profiles at $y/d \geqslant 20$ for $r = 10$ and all profiles at $r = 21$ appear to collapse to a sigmoid shape in these coordinates. The minimum of the profiles occurs near $(x/rd)/(y/rd)^{1/3} = 1.5$, while the maximum occurs near $(x/rd)/(y/rd)^{1/3} = 1.9$ Interestingly, the profiles for v'_{rms} collapse quite well at all locations. Profiles of v and v'_{rms} in the far field of the methane flames are plotted in similarity coordinates in figure 20. Not surprisingly, the similarity is entirely disrupted by the acceleration of the flow through the flame, as required by conservation of momentum (some of the effect in the $r = 10$ flame is probably due to buoyancy; see § 2.2.2). To clarify the effect of heat release, profiles of v and v'_{rms} for hot and cold cases are compared in figure 21. Non-reacting methane jet profiles are indicated by solid lines, and the flame profiles are indicated by dashed lines. A

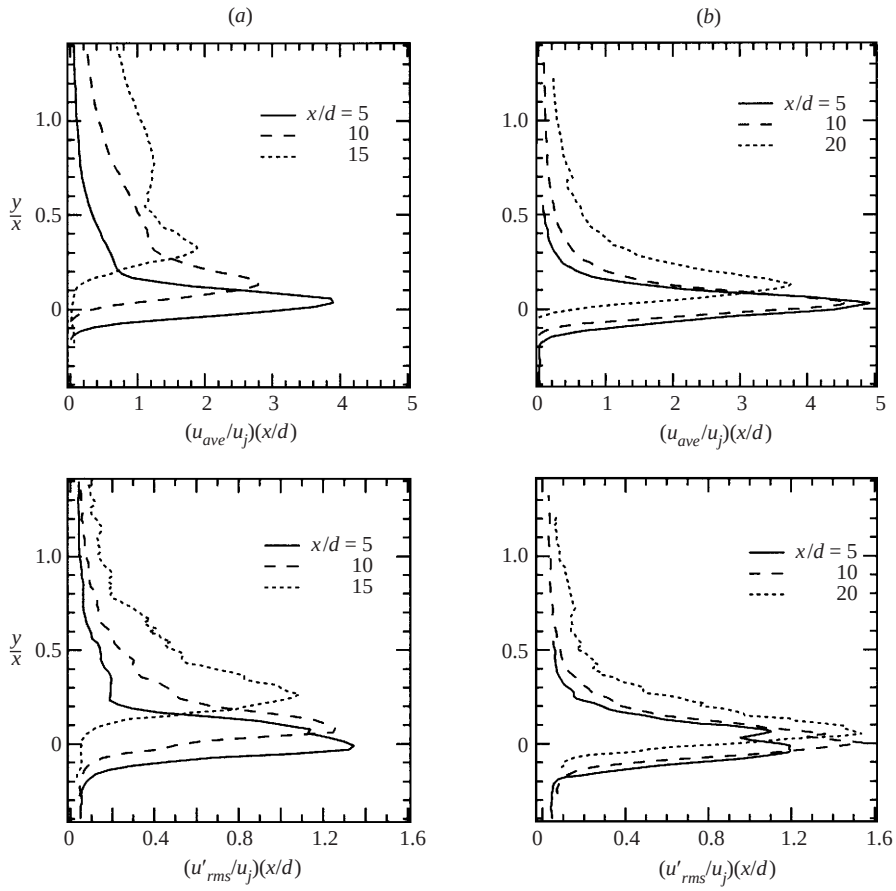

FIGURE 18. Non-reacting jet cases: velocity (top) and RMS fluctuation (bottom) profiles in near-field similarity coordinates. (*a*) $r = 10$ jet, (*b*) $r = 21$ jet.

dashed line where $\bar{v}/v_\infty = 1$ is shown for reference. Also, the location of the jet centre streamline is marked in each profile with an asterisk (*). From this it is immediately clear that the $r = 10$ flame penetrates slightly further into the crosswind than the $r = 10$ jet. An explanation of this is that heat release reduces the mass entrainment when compared to the isothermal case, which in turn reduces the jet deflection. More discussion of this is deferred until § 4.2.

In the non-reacting jets, the velocity profile asymptotically approaches the crossflow as $y/d \to \infty$ in the non-reacting jets. In the flame cases, peak values of $\bar{v}/v_\infty \approx 2.6$ at $y/d = 40$, and velocity gradients are much larger. We note that the jet centreline corresponds very well to the local maximum of $\bar{v}$ for the non-reacting case, but less so for the flame.

Profiles of v'_{rms}/u_j are shown on the bottom row of figure 21. The profiles for v'_{rms}/u_j are distinctively different in the flame and jet cases: while the jet v'_{rms}/u_j profiles are singly peaked, slightly asymmetric shapes, the flame v'_{rms}/u_j profiles are doubly peaked. As mentioned before, this is possibly a consequence of buoyancy, because this effect is not observed in the less buoyant $r = 21$ flame. It may be, however, than heat release induces fluctuations which scale with a property other than u_j (a likely candidate being S_L, the laminar flame speed), and that momentum-driven fluctuations

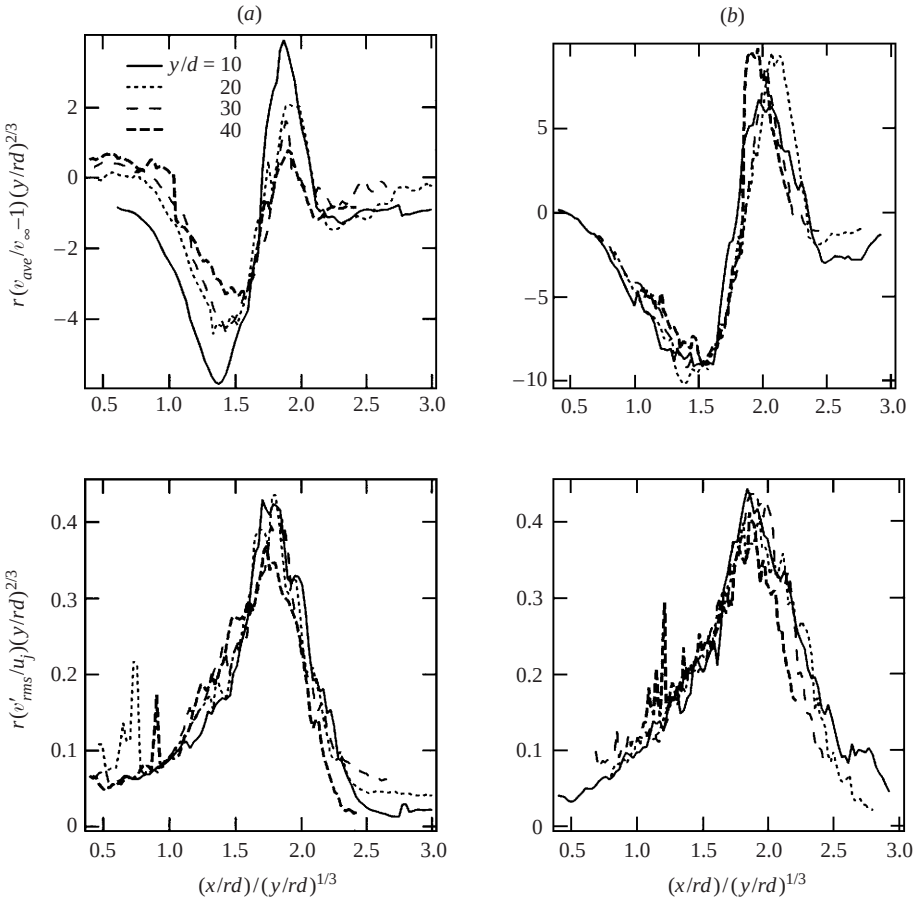

FIGURE 19. Non-reacting methane jet cases: velocity (top) and RMS fluctuation (bottom) profiles in far-field similarity coordinates. (*a*) $r = 10$ jet, (*b*) $r = 21$ jet.

dominate over heat-release fluctuations. We note that beyond the flamebase, the flame is largely non-premixed, and therefore has no inherent flame speed.

4.2. *Trajectory*

One unresolved issue from Part 1 is that, since direct measurement of entrainment coefficient is difficult, the far-field entrainment coefficient is inferred from the leading trajectory coefficient. The problem is that published trajectory data show the leading coefficient ranging at least between 1.6 and 2.1, leading to a factor-of-two uncertainty in the entrainment coefficient. In Part 1, this was temporarily resolved by using the coefficient $c_{ew} = 0.73$, based on a trajectory coefficient of 1.6 (Margason 1968; Smith & Mungal 1998), and showing consistency with the concentration data. We now revisit this issue with velocity data, for both non-reacting and burning cases.

As discussed by Kamotani & Greber (1972) and Yuan, Street & Ferziger (1999), part of the problem is that there are several possible definitions of the trajectory. Those defined as the locus of maximum concentration tend to penetrate less into the crossflow than those defined as the path traversed by the streamline passing through the centre of the jet exit. The path of this streamline is plotted for each case in figure 22. The figure plots trajectories in both *d*-normalized and *rd*-normalized

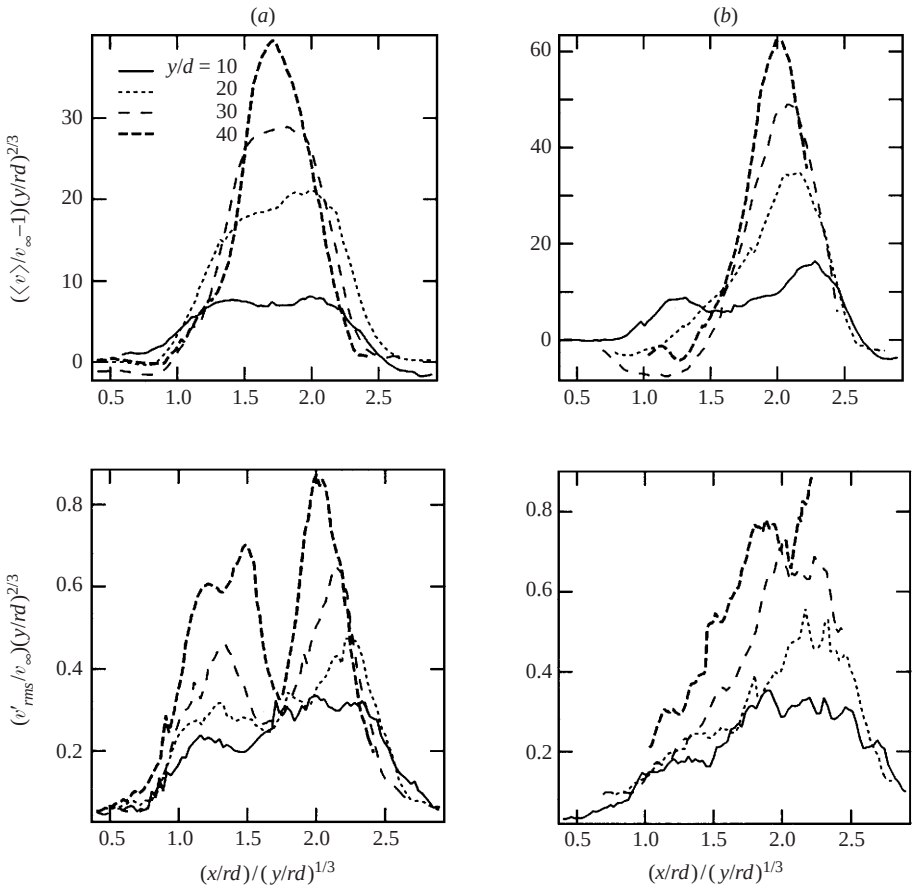

FIGURE 20. Flame cases: velocity (top) and RMS fluctuation (bottom) profiles in far-field similarity coordinates. (*a*) $r = 10$ flame, (*b*) $r = 21$ flame.

coordinates, and for comparison shows the power law given in table 4, with a leading coefficient of 2.1. The non-reacting data show at most 10% disparity in the values of x/rd for a given y/rd; however, we emphasize that the agreement is only expected for jets with $r \gg 1$.

Consistent with Kamotani & Greber's findings, the leading coefficient of the streamline trajectory is significantly different from the concentration trajectory. In a smoke visualization experiment by Margason (1968), the trajectory was found to be $x/rd = 1.6(y/rd)^{1/3}$. Furthermore, we note that the trajectory based on maximum u-component of velocity is also lower than the streamline trajectory. As shown in figure 14(*a*), the $\bar{u}$ contours bifurcate into two branches, and the branch which follows the centre streamline decays faster than the less-penetrating branch. This is a result of the entrainment into the jet from the lee side, as visualized by the streamlines shown in figures 12 and 13. The result is that the far-field maximum u trajectory (approximated by the dotted line in figure 14) has a leading coefficient of about 1.5, compared with the streamline trajectory value of about 2.1.

The far-field entrainment coefficient deduced from a leading trajectory coefficient of 2.1 is $c_{ew} = 0.32$. While this value is quite close to the free-jet entrainment coefficient of $c_{ej} = 0.32$ (Ricou & Spalding 1961), it is significantly different from the result

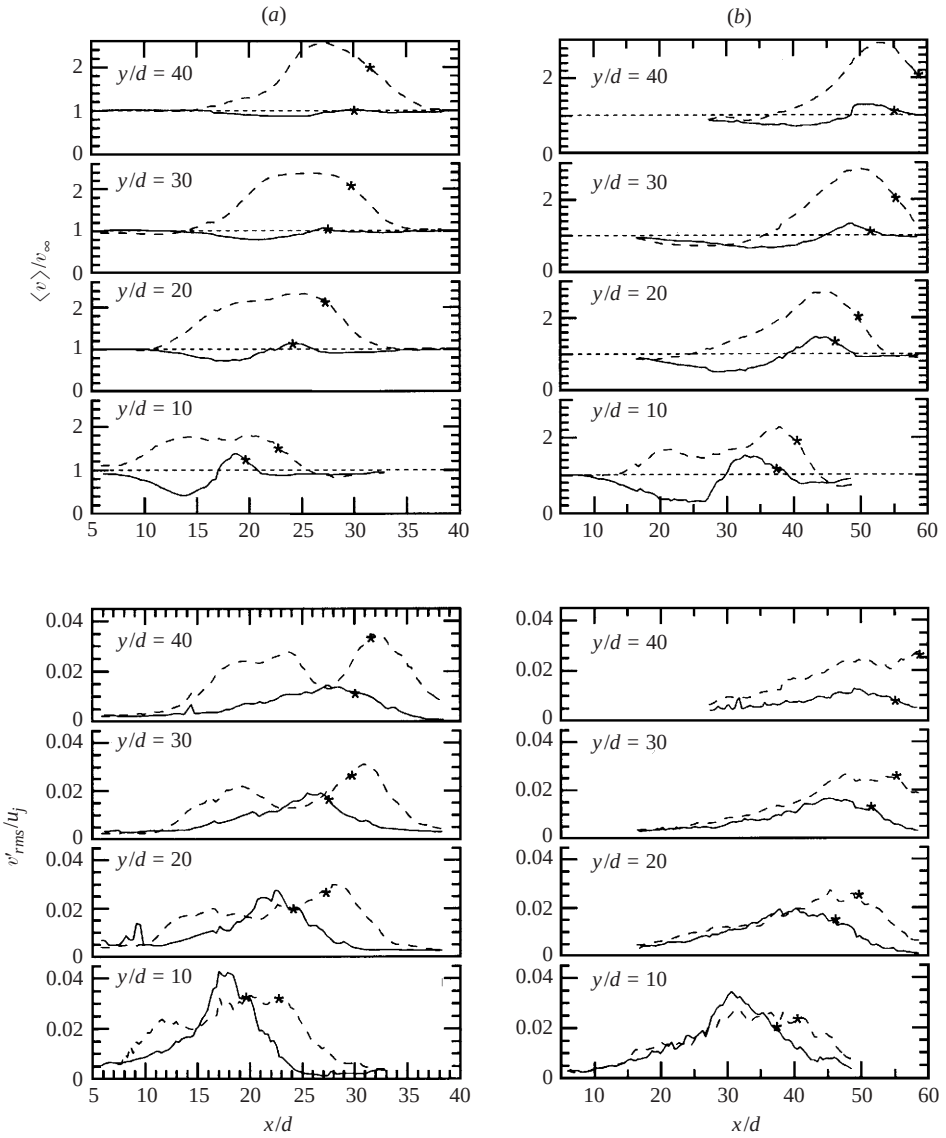

FIGURE 21. Flame cases: velocity (top) and RMS fluctuation (bottom) profiles. (*a*) $r = 10$ flame, (*b*) $r = 21$ flame. Non-reacting, solid line; reacting, dashed line.

inferred from the scalar concentration trajectory ($c_{ew} = 0.73$). This inconsistency is the direct result of oversimplification of the problem in the model constructed in Part 1, and is an example of its limitations. In other words, the scaling laws provide a useful framework for understanding this flow, but are imperfect as predictive tools.

Figure 22 also show that the flames penetrate slightly further into the crossflow than their non-reacting counterparts. The difference in x/d for a given y/d varies from +10% to +15% for $r = 10$, and from +5% to +10% for $r = 21$. The trajectories are in close agreement until the flamebase is reached, near $x/d = 10$ for the $r = 10$ case, and near $x/d = 20$ for the $r = 21$ case. At these points (the effect is clearer for $r = 21$, owing to less overlap with other data), the flame trajectory is slightly altered, and the flame centreline begins to project further into the crosswind.

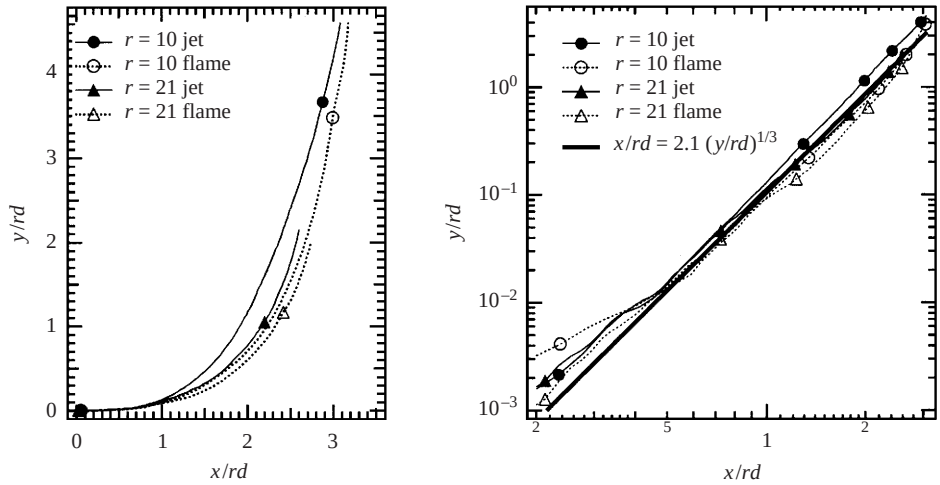

FIGURE 22. Jet and jet flame trajectories, based on jet-exit centre streamline, in *rd*-normalized coordinates.

This observation can be explained as a result of reduced mass entrainment rate in the flame cases. As suggested in Part 1 of this paper, the rate of jet deflection is directly related to the rate of entrainment:

$$\frac{x_c}{rd} = \left(\frac{3}{c_{ew}}\frac{y_c}{rd}\right)^{1/3}. \tag{4.3}$$

Here, c_{ew} is an entrainment coefficient; therefore, less deflection implies lower crossflow entrainment, integrated over the jet history. Becker & Yamazaki (1978) found that entrainment rates of momentum-driven jet flames were reduced by a factor of two compared to non-reacting jets. Clemens & Paul (1995) found that entrainment rates in the near field of a hydrogen–air jet were reduced as a result of heat release in the flammable layer enveloping the jet, an effect which is analogous to the density-ratio effect found in mixing layers. Assuming that these observations are applicable to transverse jets, one expects the flame to penetrate further into the crossflow. The difference should not be dramatic, however, due to the significant mixing that occurs before the flamebase, and the cubic relationship between trajectory and entrainment coefficient.

4.3. *Centreline u-velocity*

In Part 1 of this paper, scaling laws for characteristic jet velocity were derived. Here we compare these scaling laws with experimental data along the centre streamline of the jet. However, a caveat is warranted. The profile data shown in §4.1 demonstrate that characteristic velocities (i.e. maximum $\bar{u}$ or $\bar{v}$ deficit) do not always correspond to the jet centre streamline.

As given in table 3, the scaling law for $\bar{u}_c$ in the near field is

$$\frac{\bar{u}_c}{u_j} = \frac{c_{un}}{c_{ej}}\left(\frac{\rho_j}{\rho_\infty}\right)^{1/2}\left(\frac{x}{d}\right)^{-1} = \frac{1}{r}\frac{c_{un}}{c_{ej}}\left(\frac{\rho_j}{\rho_\infty}\right)^{1/2}\left(\frac{2}{c_{ej}}\frac{y}{rd}\right)^{-1/2} \tag{4.4}$$

(the second equality is obtained using the trajectory, given in the table). In the far

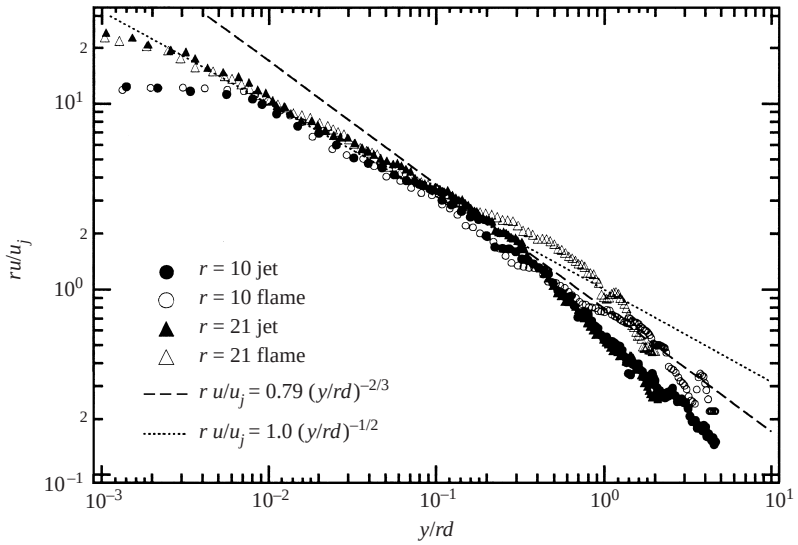

FIGURE 23. $r\bar{u}/u_j$ versus y/rd (crossflow direction) along jet trajectory streamline. A $-1/2$ power-law fit to near-field data is shown, as is the $-2/3$ power law for the far field using $c_{ew} = 0.73$ and $c_{uf} = 2$. Far-field discrepancy is at least in part due to bifurcation of u contours, shown in figures 14 and 16.

field, the scaling law is

$$\frac{\bar{u}_c}{u_j} = \frac{c_{uf}}{(9c_{ew})^{1/3}}\frac{1}{r}\left(\frac{\rho_j}{\rho_\infty}\right)^{1/2}\left(\frac{y}{rd}\right)^{-2/3}. \tag{4.5}$$

Therefore $r\bar{u}_c/u_j$ plotted versus y/rd should collapse to a single curve with slope $-1/2$ in the near field and $-2/3$ in the far field (outside of the potential core region). The similarity variable $r\bar{u}_c/u_j$, *obtained along the streamline trajectory* is plotted for all four cases in figure 23. The non-reacting jet data collapse to a single curve, with deviation less than $\pm 8\%$ over the entire range; the portion of the flames upstream of the flamebase collapses to the same curve, as expected. For comparison, a curve fit to the far-field scaling law with $c_{ew} = 0.73$ and $c_{uf} = 2$ is shown. Also, by substituting the near-field trajectory $y/rd = [(2/c_{ej})(x/rd)]^{1/2}$ into the near-field scaling law, the near-field velocity decay law is $r\bar{u}_c/u_j = c(y/rd)^{-1/2}$; with $c = 1$, agreement with the data in the range $0.01 < y/rd < 0.2$ is very good. Qualitatively, the $\bar{u}_c$ data for non-reacting jets look very much like the data for concentration shown in Part 1 insofar as a transition from near-field to far-field scaling is observed. However, it appears that the slope of -1 is a better approximation to the data than the $-2/3$ slope predicted by the scaling law, as a direct consequence of the trajectory definitions discussed in the previous section.

The effect of heat release in both cases is to increase the velocity, by a factor which increases at first, and then appears to relax, with downstream distance. The maximum value of the ratio appears to be about 2.6, which occurs at $x/d = 23$ for the $r = 10$ case, and $x/d = 43$ for the $r = 21$ case. This behaviour is similar to the behaviour of centreline temperature in flames, where temperature rises until $3/4L_f$, then decreases afterwards (Takagi, Shin & Ishio 1981).

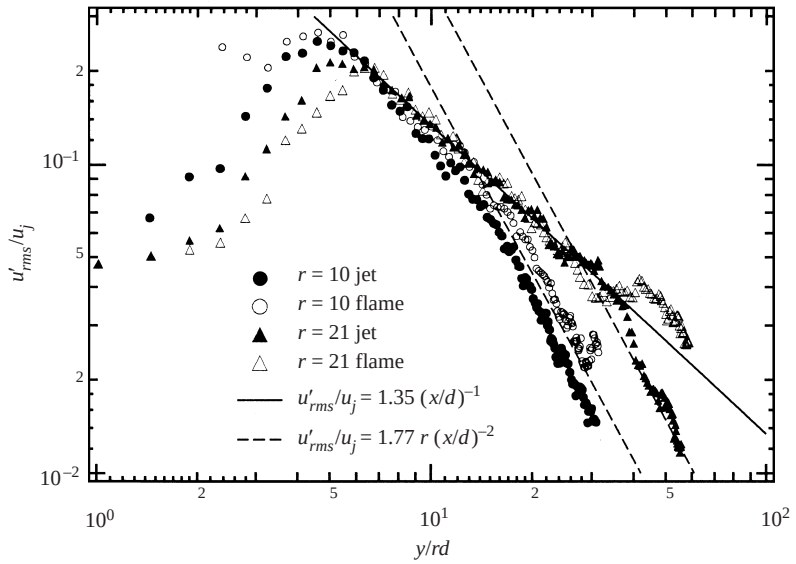

FIGURE 24. u'_{rms}/u_j, along jet trajectory streamline, versus x/d (jet direction). Scaling laws using $c_{ej} = 0.32$, $c_{ew} = 0.32$, $c_{u'n} = 0.58$, and $c_{u'f} = 0.76$ are shown for comparison.

4.3.1. *Centreline velocity fluctuations*

Turbulence fluctuations are generally expected to scale with local characteristic velocity differences. Beyond the jet potential core region, both $\bar{u}_c/u_j$ and $(v_\infty - \bar{v}_c)/v_\infty$ have the same scaling laws. Under the assumption that turbulence fluctuations are a constant multiple of these characteristic velocity differences, we expect u'_{rms} and v'_{rms} to obey the same scaling law as $\bar{u}_c$ and $v_\infty - \bar{v}_c$, as given above. That is, we expect to find fluctuations proportional to x^{-1} in the near field, and $y^{-2/3}$ in the far field.

This behaviour is confirmed by the data. In the near field, a fit to the data (figure 24) shows very good agreement with x^{-1}. The far-field fit to x^{-2} does not work as well, but this is largely due to deviation of the actual trajectory from the predicted trajectory. When plotted versus y/rd (figure 25), the agreement is very good. The collapse of the non-reacting curves in similarity coordinates is also very good, which highlights the effect of heat release on the fluctuations. The RMS fluctuation jumps by at least 50% at the flamebase location, due to the dilation at the base of the partially premixed flame.

Scaling laws for u'_{rms} which closely match the data for the non-reacting jets can be obtained for each regime by assuming constant turbulence intensity. Since the flow transitions from jet-like to wake-like, however, it seems reasonable that the turbulence intensity may have different asymptotic values in the near field and far field.

In the near field, the scaling law for the fluctuation along the centre streamline is then

$$\frac{u'_{rms}}{u_j} = \frac{c_{u'n}}{c_{ej}} \left(\frac{\rho_j}{\rho_\infty}\right)^{1/2} \left(\frac{x}{d}\right)^{-1}, \tag{4.6}$$

where we have multiplied (4.4) by a characteristic turbulence intensity, $c_{u'n}/c_{un}$. Wygnaski & Fiedler (1969) reported a value of 0.29 in free jets. Using the density of methane, and $c_{ej} = 0.32$, we obtain exactly the same value when using the leading coefficient of 1.35 shown in figure 24.

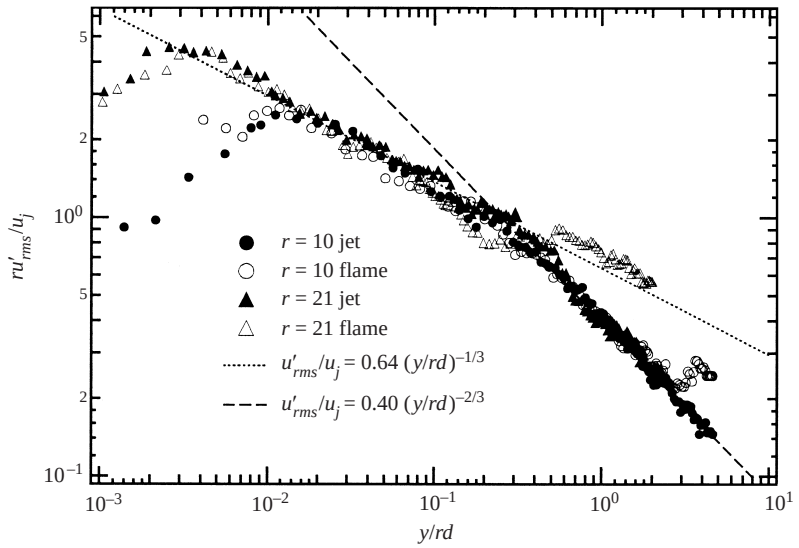

FIGURE 25. ru'_{rms}/u_j along jet trajectory streamline, versus y/rd (crossflow direction). Scaling laws using $c_{ej} = 0.32$, $c_{ew} = 0.32$, $c_{u'n} = 0.58$, and $c_{u'f} = 0.76$ are shown for comparison.

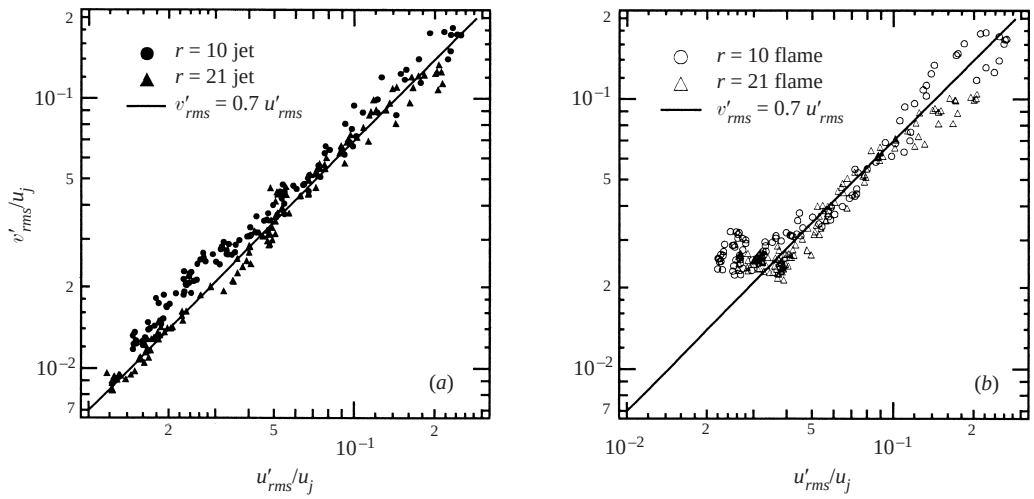

FIGURE 26. v'_{rms} fluctuation versus RMS u'_{rms} fluctuation along jet trajectory streamline: (*a*) non-reacting cases, (*b*) methane flame cases. Straight line is $v'_{rms} = 0.7u'_{rms}$.

In the far field, the scaling law for the fluctuation along the centre streamline is

$$\frac{u'_{rms}}{u_j} = \frac{c_{u'f}}{(9c_{ew})^{1/3}} \frac{1}{r} \left(\frac{\rho_j}{\rho_\infty}\right)^{1/2} \left(\frac{y}{rd}\right)^{-2/3}, \tag{4.7}$$

where we have multiplied (4.5) by $c_{u'f}/c_{uf}$. Typical values of this ratio reported in the literature are near 0.38 based on the typical turbulence intensities reported in wakes. Taking $c_{uf} = 2.0$, $c_{ew} = 0.73$ and the leading coefficient of 0.40 from figure 25, we obtain a characteristic turbulence intensity $c_{u'f} = 1.0$.

In figure 26, we test the supposition that $v'_{rms} \sim u'_{rms}$ by plotting these quantities against each other at each sampling point along the centre streamline. For the non-

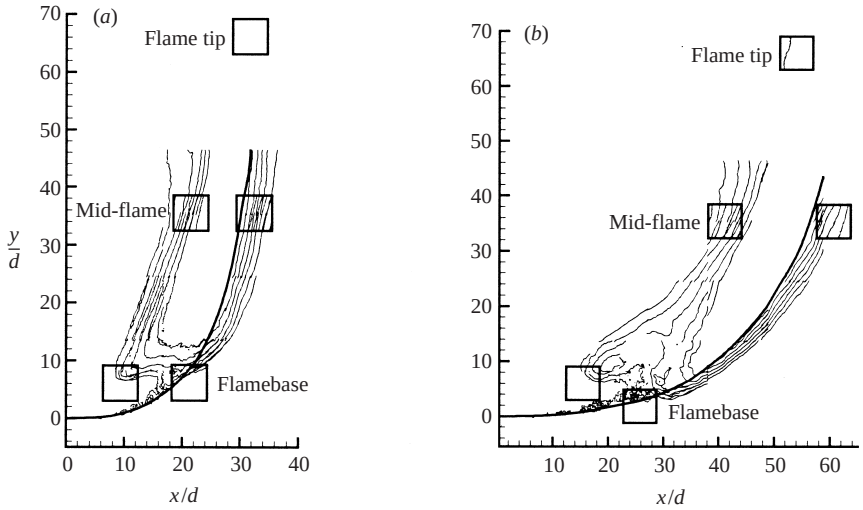

FIGURE 27. Simultaneous PIV/OH imaging windows: (*a*) $r = 10$ case; (*b*) $r = 21$ case. Centre streamline from PIV experiments (slightly different conditions) and contours at $\bar{v}/v_\infty = 1.2$, 1.4, 1.6, 1.8, and 2.0 are shown for comparison. Contours shown in PIV/OH windows show good matching to whole-field PIV experiment results. Single contour at flame tip in $r = 21$ case corresponds to $\bar{v}/v_\infty = 2.0$.

reacting jets, nearly all the data fall within $\pm 50\%$ of the line $v'_{rms} = 0.7u'_{rms}$. For the flames, however, deviation from this linear relationship is observed for low u'_{rms}, corresponding to data points in the flame, with the deviated region approximately obeying $v'_{rms}/u_j \approx 0.025$.

5. Results: OH PLIF imaging

Figure 27 shows the regions where OH PLIF images were obtained simultaneously with PIV data; the centre streamlines and $\bar{v}$ contours from the PIV experiments are shown for reference. Owing to the additional experimental complexity, only five imaging locations were selected for study: the lee and windward flamebase, the lee and windward mid-flame, and the flame tip.

5.1. *Instantaneous OH structure*

A representative selection of OH PLIF images in each of the five viewing regions are shown in figure 28 for $r = 10$ and in figure 29 for $r = 21$. The structure of the flame implied by these images is markedly different near the flamebase compared to elsewhere in the field. At the flamebase, the OH field is wrinkled, and is often broken into multiple islands and occasionally shows pockets of no signal (although these last two are possibly an artifact of taking a two-dimensional slice through a three-dimensional field). At the lee-side flamebase, the OH field is up to 3 cm thick, which suggests that there is a wide flammable region upstream of the flame front. While this result is supported by the observation of blue emission at the flame base, it is not particularly surprising, since the lifted flame allows the jet to premix fuel and air upstream of the flamebase. On the windward side, the flamebase is often broken into multiple islands, which is consistent with the high turbulence intensities observed along the windward edge of the flame in the greyscale maps shown previously in

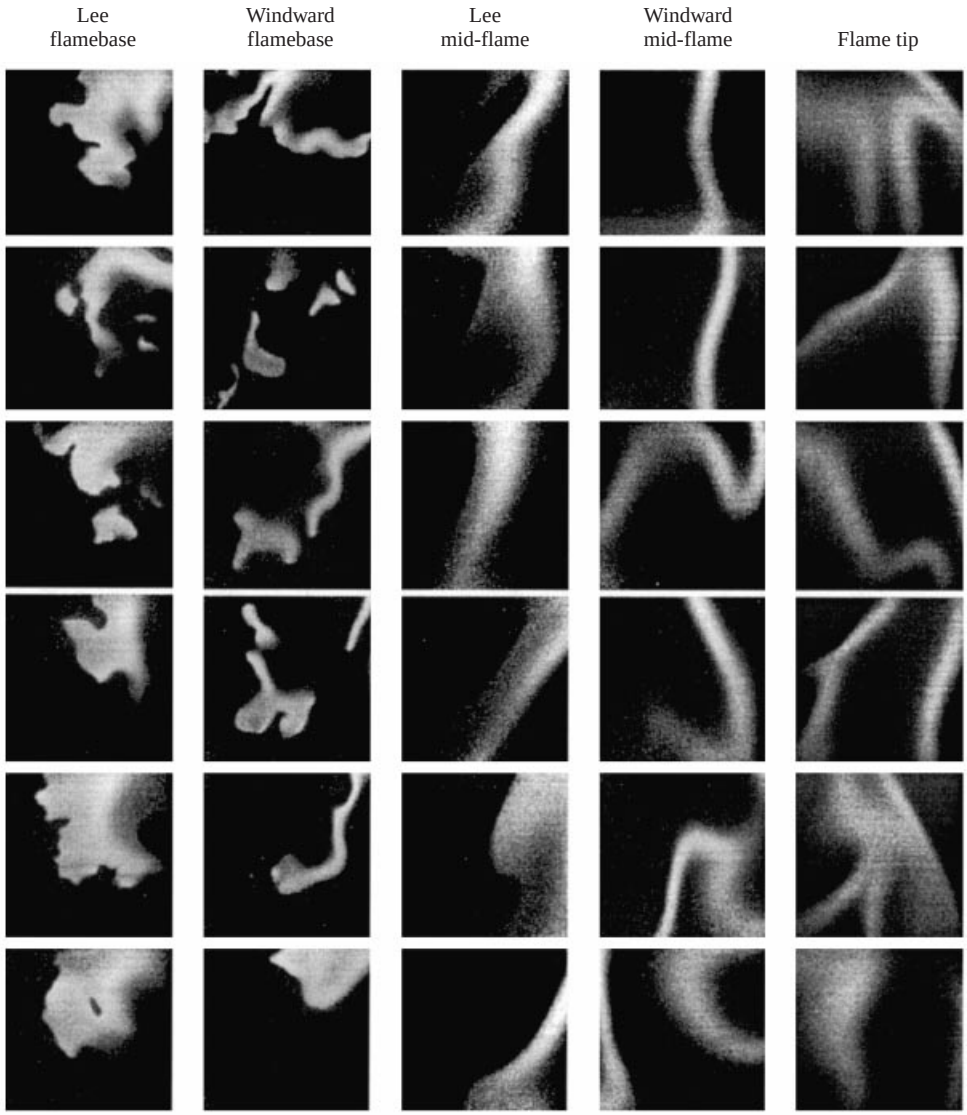

FIGURE 28. A representative selection of OH images, $r = 10$ case.

figure 15. The degree of wrinkling appears slightly greater in the $r = 21$ case, which has $Re = 12\,800$, compared to the $r = 10$ case with $Re = 6000$.

It might be hypothesized that flame front curvature introduces an important component to the local stretch rate, and hence a mechanism for local extinction. Flame front curvature (inverse radius of curvature) can be visually estimated to reach values as high as $10\,\mathrm{cm}^{-1}$ (the smallest OH wrinkles and thinnest slivers are about 2 mm across, and the radius of curvature is half this amount). Presuming that the flame-normal velocities are near $S_L = 40\,\mathrm{cm\,s}^{-1}$, this implies stretch rates up to $400\,\mathrm{s}^{-1}$ along the flame. This value is about one-fourth the extinction stretch rate of $1772\,\mathrm{s}^{-1}$ for stoichiometric methane–air flames found in axisymmetric laminar counterflow experiments (Law *et al.* 1986). However, this is only one component of the total stretch. Hence, based on these images, local curvature due to small-scale distortion

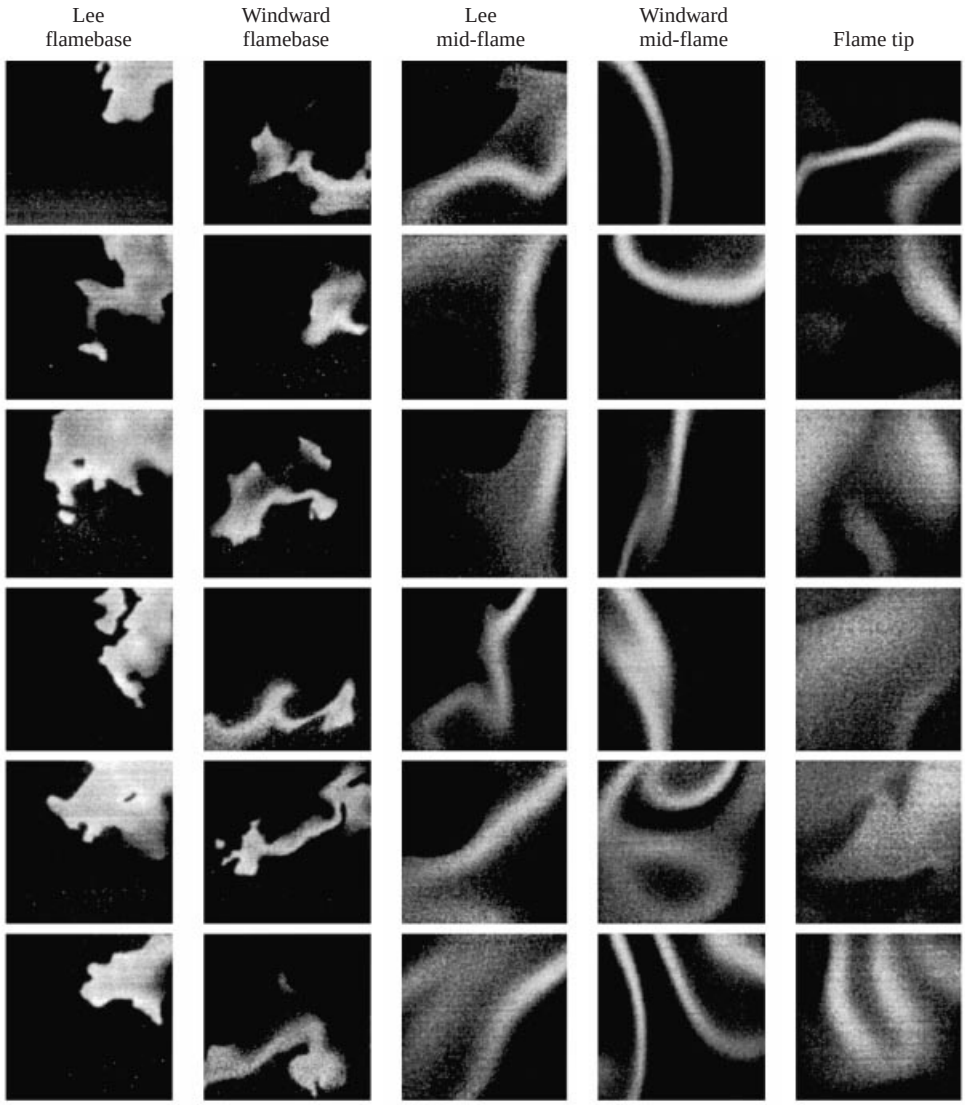

FIGURE 29. A representative selection of OH images, $r = 21$ case.

is expected to be a factor, but perhaps not the governing mechanism, of lifted flame stabilization.

In contrast to the flamebase, at the mid-flame locations, the character of the OH field appears to be much more laminar and sheet-like. Because heat release tends to increase dynamic viscosity and reduce the density of the fluid, the Reynolds number is effectively reduced. On the assumption that a characteristic momentum flux of the flow $\rho u^2 \delta^2$ is constant, it can be shown that the Reynolds number is

$$Re = Re_o \frac{\mu_o}{\mu(T)} \left(\frac{\rho_o}{\rho(T)} \right)^{-1/2}. \tag{5.1}$$

Since $\mu \sim T^{0.7}$ for most gases, and $\rho \sim T^{-1}$, $Re \sim T^{-1.2}$. For a temperature ratio of 7, this represents up to a factor of 10 decrease in Reynolds number compared to

the non-reacting case. Hence the $r = 10$ and $r = 21$ cases are reduced to equivalent Reynolds number of only 630 and 1330, respectively. In this particular flow, therefore, one of the effects of heat release is a strong laminarization of the flow, as evidenced by the OH images. This is an unavoidable consequence of the limited scale of the experiment and the use of a methane flame, which tends to blow off at lower jet exit speeds than hydrogen or ethylene.

At the windward mid-flame location, the flame sheet is occasionally distorted by large-scale vortices, apparently from the jet shear layer. Also, the flame appears to be somewhat thinner than on the lee of the jet. This is most likely a consequence of the streamline patterns around the jet, as shown in figure 11. On the windward side, the flame experiences compressional strain in the viewing plane, but on the lee it experiences compressive strain out-of-plane, which is expected to thicken the flame in this cross-section. In general, the OH field structure in the mid-flame regions is often consistent with diffusion 'flamelet' structure (Peters 1984), although the OH filaments are sometimes quite thick, implying low scalar dissipation and strain rates. However, this might not be the case in higher-*Re* flames – Clemens, Paul & Mungal (1997) studied a hydrogen–air diffusion flame up to $Re = 150\,000$, and found that the degree of wrinkling increases with increasing Reynolds number.

Finally, the flame tip shows evidence of thin sheet-like regions as well as broad homogeneous regions. Whether the broad OH regions are simply OH which lingers in high-temperature regions or are evidence of reaction occurring in this region is unclear, because of the Dahmköhler number effects described in § 2.3.3. When sheet-like layers do appear, their orientation is more random than at mid-flame locations.

5.2. *Flow/flame interaction at the flamebase*

Recent work on the phenomenon of turbulent lifted-flame stabilization by Muñiz & Mungal (1997) and Schefer & Goix (1998) has found that velocities conditionally sampled just upstream of the instantaneous flame front are $O(S_L)$, ranging from 0 to $3S_L$. The findings have prompted analogies of the flamebase with triple flames, which are laminar flames propagating into a uniform velocity field with a weak mixture fraction gradient (Dold 1989). The 'triple flame' appellation comes from the tribrachial structure of the flame, which has two premixed branches (one rich, one lean), and a diffusion flame tail. As mixture fraction gradient is increased, however, the flame folds into a single flame. These flames are collectively known as 'leading edge' flames.

An analysis and direct numerical simulations by Ruetsch, Vervisch & Liñan (1995) show that the flow approaching a triple flame slows down as it approaches the flamefront, due to diverging streamlines upstream of the flamefront. The flow speed at the flamefront along the stoichiometric streamline is S_L; however, a few flame-widths upstream of this point, the flow speed is proportional to $(\rho_u/\rho_b)^{1/2}S_L$ (subscripts u and b refer to unburned and burned gases, respectively). Therefore the triple flame can propagate into the oncoming mean flow faster than S_L. Furthermore, their analysis shows that the flow speed far behind the flame is also proportional to $(\rho_u/\rho_b)^{1/2}S_L$; from their data, it appears that the proportionality constant for the flow in front of the flame is less than unity, but for the flow behind the flame, the constant is very nearly unity.

Owing to fluctuating velocities and a contorted mixture fraction field upstream of a lifted turbulent flame, the flamebase is highly unlikely to be a triple flame. However, an interesting aspect of the Ruetsch *et al.* (1995) analysis is that it makes no assumption of a triple-flame structure – it simply requires that the streamlines are

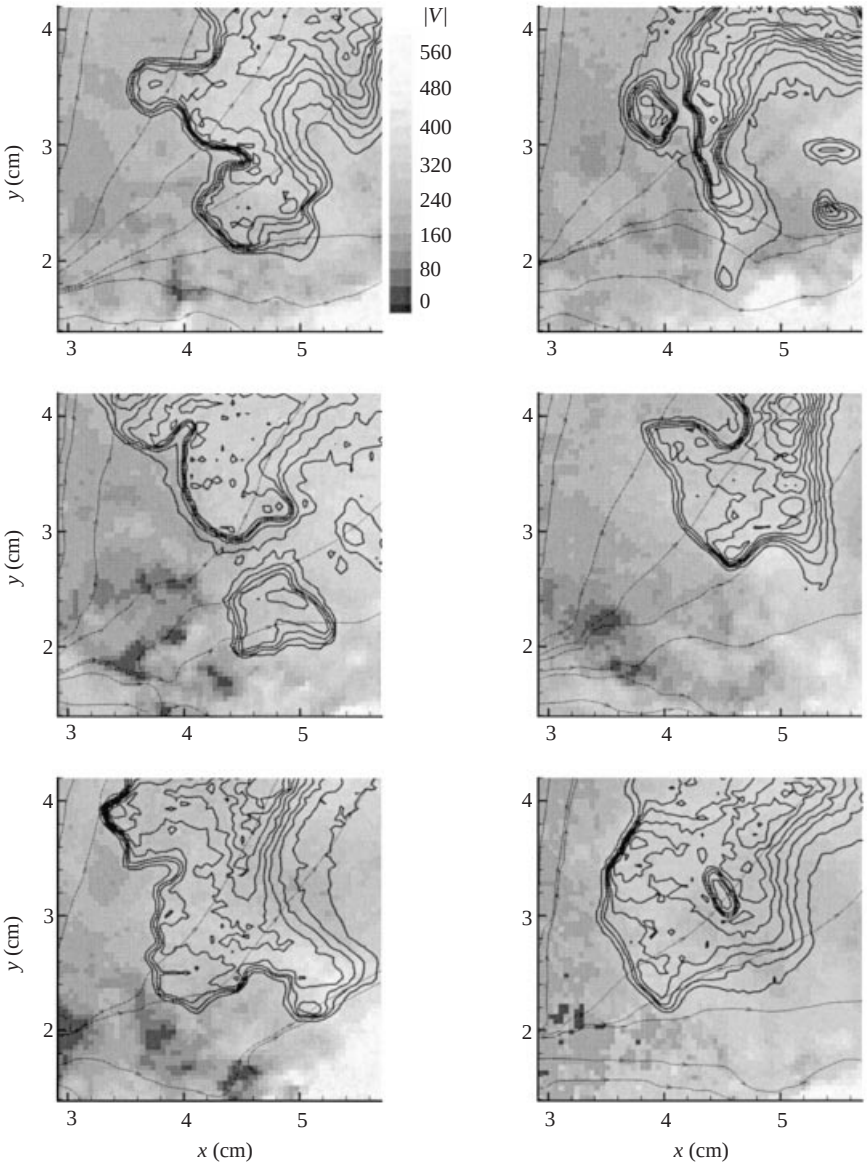

FIGURE 30. A representative selection of instantaneous flow patterns, $r = 10$ lee flamebase. Cases correspond to OH images shown in figure 28. Greyscale contours show velocity magnitude, in cm s^{-1}. Heavy black-line contours show OH signal levels. Streamlines integrated from velocity field are overlaid.

unconstrained, and thus may divert around a finite region of heat release. In other words, the analytical result should be generally applicable to the turbulent flame base, regardless of structural details.

Figures 30 and 31 demonstrate that streamline divergence does indeed appear just upstream of the $r = 10$ instantaneous flamebase. The greyscale map is velocity magnitude, overlaid with streamlines, with the black line contours indicating OH signal. It is emphasized, however, that the streamlines are not pathlines through the

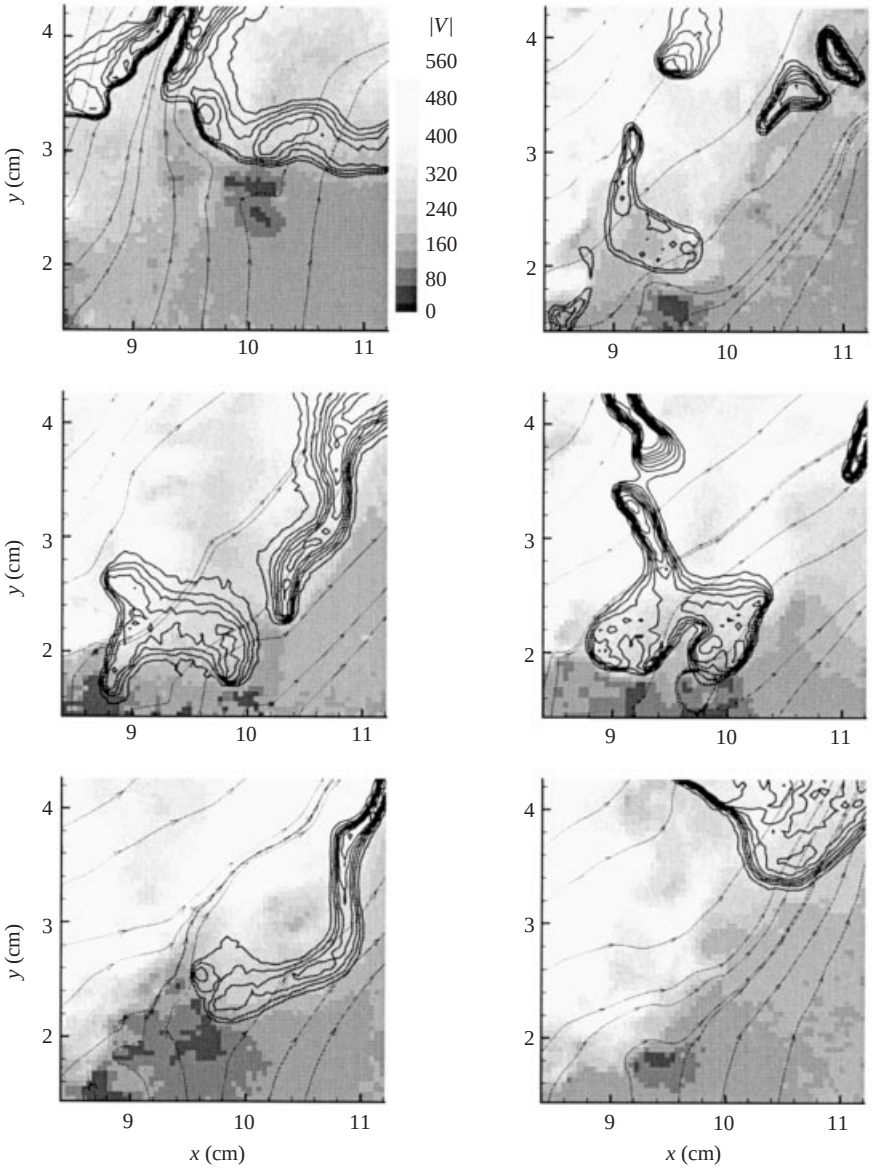

FIGURE 31. As figure 30 but for windward flamebase.

flame, due to unsteadiness. Samples from the $r = 21$ jet have a similar character (Hasselbrink 1999).

Statistical measures of this interaction of flame and flow at the flamebase were obtained in previous work (Hasselbrink & Mungal 1998*a*, *c*), which attempted to account for unsteadiness at the base of coflowing lifted flames by subtracting the local flame velocity from the approaching flow speed. Although in this experiment there was difficulty dealing with three-dimensional effects and out-of-plane motion of the flamefront, a linear correlation of flamefront and fluid velocities (in the lab frame) was observed, and the most likely relative flow velocity just upstream of the instantaneous flamebase was found to be near the laminar flame speed. In other

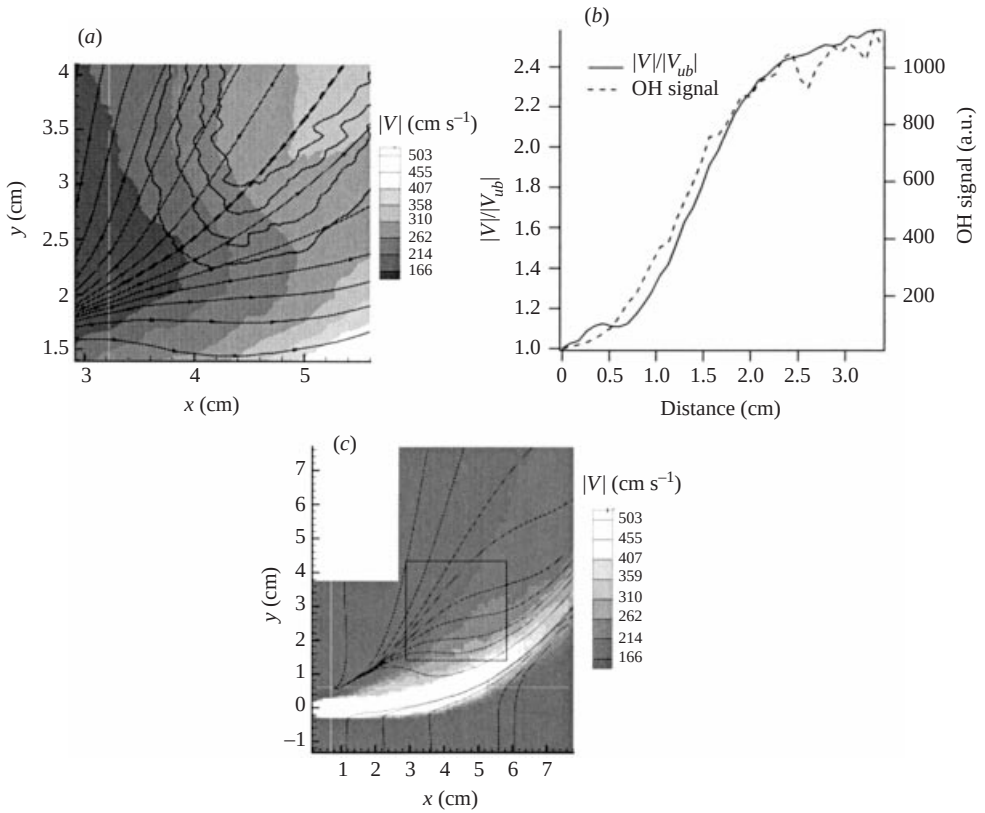

FIGURE 32. Average speed through the $r = 10$ lee flamebase. (*a*) Greyscale map of velocity magnitude, overlaid with streamlines and black-line contours of OH signal. Results of 110 frame ensemble average. (*b*) Plot of velocity and OH signal through dashed streamline in (*a*); $|V_{ub}| = 127\,\mathrm{cm/s}$. (*c*) Non-reacting case, shown for comparison. Inset box corresponds to region imaged in (*a*).

words, the results suggested that the flamefront indeed recedes when the oncoming flow exceeds the laminar flame speed, and advances when the oncoming flow is slower than the laminar flame speed.

As mentioned previously, based on the analysis of Ruetsch *et al.* (1995), the acceleration through the flame base is expected to be such that the burned fluid velocity exceeds the unburned fluid velocity by a factor proportional to the square root of the temperature ratio. For methane flames, this is a factor of 2.7, presuming the adiabatic flame temperature is reached. Figure 32(*a*) shows a greyscale map of the velocity magnitude for the ensemble-averaged flow at the $r = 10$ lee-side flamebase; the edge of the main jet flow is visible as a white region at the lower right corner of the domain. The greyscale contours are overlaid with black line contours of the average OH signal, as well as averaged streamlines. A plot of the OH signal and velocity magnitude through the dashed streamline in figure 32(*b*) shows that the flow speed increases by a factor of 2.5 while passing through the flamebase. The velocity magnitude field and streamlines for the non-reacting case are shown in (*c*) for comparison. The lack of a bright region in the upper right corner of the inset box (corresponding to the simultaneous imaging region) indicates that the acceleration does not occur in the non-reacting case. Since the streamline pattern changes somewhat, direct comparison of acceleration along the same streamline is not possible.

6. Summary and conclusions

Turbulent transverse jets at high jet-to-crossflow blowing ratios have been investigated using both analytical and experimental techniques, with the primary goal of understanding the overall structure of the velocity field, and how it is influenced by combustion heat release. Algebraic scaling laws for the simplest case of non-reacting jets at high r were developed, and agreement with existing concentration and velocity data was demonstrated.

In order to further test the scaling laws, and to assess the influence of combustion heat release, velocity field measurements have been obtained in the symmetry plane for methane jets and flames of two blowing ratios, $r = 10$ and $r = 21$. In addition, investigations into the instantaneous and statistical interactions of flow and flame have also been performed, using simultaneous PIV/OH PLIF imaging at five locations in each flame: at the lee and windward flamebases, at the lee and windward edges of the flame about halfway between the flame base and the flame tip, and at the flame tip.

Major results of the present work are as follows:

(i) Scaling laws developed in Part 1 for strong transverse jets provide a reasonably good framework for predicting the scaling of the streamline trajectory, and show good collapse of mean velocity profiles and RMS fluctuation profiles, for the $r = 10$ and $r = 21$ cases studied here. Scaling laws derived for centreline u-velocity along the trajectory, however, are not as accurate because the locus of maximum $\bar{u}$ does not follow the streamline trajectory in the far field. The crossflow (v) component of velocity relaxes rapidly to the crossflow speed in the absence of combustion heat release.

(ii) An apparent 'source' exists in the time-averaged two-dimensional flow in the symmetry plane. A similar result was found by Kelso *et al.* (1996) for jets issuing from a wall. The source is located in the lee of the jet, centred at about $(x/d, y/d) = (1, 1)$ in the laboratory coordinate system. The source corresponds to a region of large $-\partial w/\partial z$, indicating that there is compressive strain, i.e. opposed flow, in the out-of-plane direction on the lee side. In contrast, on the leading edge, $\partial w/\partial z$ is not nearly as large, indicating that much of the crossflow approaching the leading edge is entrained into the jet, rather than diverted around it. This is consistent with the observation that flow speeds reach zero at the 'source' in the lee, but the crossflow slows by only about 40% as it approaches the leading edge of the jet (the effect being slightly more pronounced in the case of the flame). However, this 40% reduction also indicates that some out-of-plane acceleration is present, which implies that pressure is higher than ambient at the leading edge of the jet.

(iii) The centre streamline from the jet nozzle follows a power-law trajectory when normalized by the outer length scale, rd. The power-law exponent is $1/3$, as predicted by scaling laws, and the leading coefficient measured is 2.1 to within experimental uncertainty. Combustion heat release causes a slight deviation in the trajectory, such that the jet penetrates slightly further into the crossflow; this behaviour is consistent with the findings of Becker & Yamazaki (1978) that the entrainment coefficient for flames is lower than for non-reacting jets.

(iv) Combustion heat release accelerates the flow within the heated region. As the flame tip is approached, maximum $\bar{v}/v_\infty \approx 2.7$. This factor may be a simple result of momentum conservation. Rehm & Clemens (1999) and Muñiz (2001) have found that the characteristic width of turbulent jet flames does not change dramatically compared with non-reacting jets. Therefore, the momentum flux per unit area must

be approximately the same for the two flows, and since $J \sim \rho v^2 A$, it follows that ρv^2 is nearly equivalent in the two cases. Therefore if density drops by a factor of T_f/T_o, flow speed must increase by $(T_f/T_o)^{1/2}$. An intriguing implication of this result is that the mass entrainment, $\dot{m} \sim \rho u A$, is reduced by the factor $(T_f/T_o)^{1/2}$. An investigation of the reduction of entrainment due to heat release, via direct measurement of entrainment into the jet, is currently underway (Han, Miraflor & Mungal 1999).

(v) Regions of high OH fluorescence near the flamebase are highly contorted, are broad (up to 3 cm across), and are characterized by steep gradients of OH on the leading edge, but fairly uniform OH signal within the OH zones. The degree of brokenness and wrinkling is somewhat greater in the higher r (and higher Re) case. These observations suggest significant partial premixing upstream of the flamefront. In contrast, the OH field is significantly smoother at the mid-flame and tip imaging locations. This behaviour is probably partly due to the decrease by a factor of about 10 in the effective Reynolds number of the flow, which is a side effect of heat release. However, it also suggests that by mid-flame, all premixed air has been consumed and the flame is essentially a diffusion flame.

We would like to acknowledge many motivational discussions with J. E. Broadwell, as well as the assistance of L. Muñiz, L. Su, D. Han, and R. Miraflor in the experimental portion of the work. We also acknowledge the support of the Gas Research Institute, R. V. Serauskas, Technical Monitor.

REFERENCES

Andreopoulos, J. & Rodi, W. 1985 On the structure of jets in crossflow. *J. Fluid Mech.* **138**, 93–127.

Ashforth-Frost, S., Dobbins, B. N., Jambunathan, K., Wu, X. & Ju, X. Y. 1993 Comparison of interrogation methods for particle image velocimetry. In *Proc. SPIE – The Int. Soc. for Optical Engng*, pp. 478–489. Society of Photo-Optical Instrumentation Engineers, Bellingham, WA, USA.

Barenblatt, G. I. 1996 *Scaling, Self-similarity, and Intermediate Asymptotics.* Cambridge University Press.

Barlow, R. S. & Collignon, A. 1991 Linear LIF measurements of OH in nonpremixed methane-air flames: When are quenching corrections unnecessary? *AIAA Paper* 91-0179.

Becker, H. A. & Yamazaki, S. 1978 Entrainment, momentum flux and temperature in vertical free turbulent diffusion flames. *Combust. Flame* **33**, 123–149.

Buch, K. A. & Dahm, W. J. 1998 Experimental study of the fine-scale structure of conserved scalar mixing in turbulent shear flows. Part 2. Sc $\approx$ 1. *J. Fluid Mech.* **364**, 1–29.

Champagne, F. H. 1978 The fine-scale structure of the turbulent velocity field. *J. Mech.* **86**, 67–108.

Chassaing, P., George, J., Claria, A. & Sananes, F. 1974 Physical characteristics of subsonic jets in a cross-stream. *J. Fluid Mech.* **62**, 41–64.

Chen, C. J. & Rodi, W. 1980 *Vertical Turbulent Buoyant Jets: A Review of Experimental Data.* Pergamon.

Cheremisinoff, N. P. & Cheremisinoff, P. N. 1984 *Hydrodynamics of Gas-Solids Fluidization.* Gulf.

Clemens, N. T. & Paul, P. H. 1995 Effects of heat release on the near field flow structure of hydrogen jet diffusion flames. *Combust. Flame* **102**, 271–284.

Clemens, N. T., Paul, P. H. & Mungal, M. G. 1997 The structure of OH fields in high Reynolds number turbulent jet diffusion flames. *Combust. Sci. Tech.* **129**(1–6), 165–184.

Coelho, S. L. V. & Hunt, J. C. R. 1989 The dynamics of the near field of strong jets in crossflows. *J. Fluid Mech.* **200**, 95–120.

Dold, J. 1989 Flame propagation in a nonuniform mixture: analysis of a slowly varying triple flame. *Combust. Flame* **76**, 71–88.

Dowling, D. R. & Dimotakis, P. E. 1990 Similarity of the concentration field of gas-phase turbulent jets. *J. Fluid Mech.* **218**, 109–141.

Fearn, R. L. & Weston, R. P. 1974 Vorticity associated with a jet in a cross flow. *AIAA J.* **12**, 1666–1671.

Fric, T. F. & Roshko, A. 1994 Vortical structure in the wake of a transverse jet. *J. Fluid Mech.* **279**, 1–47.

Gogineni, S., Goss, L. & Roquemore, M. 1995 Manipulation of a jet in a crossflow. *Expl. Therm. Fluid Sci.* **16**, 209–219.

Gollahalli, S. R., Brzustowski, T. A. & Sullivan, H. F. 1975 Characteristics of a turbulent propane diffusion flame in a cross-wind. *Trans. Can. Soc. Mech. Engng* **3**, 205–214.

Gomez, A. & Rosner, D. E. 1993 Thermophoretic effects on particles in counterflow laminar diffusion flames. *Combust. Sci. Tech.* **89**(5–6), 335–362.

Han, D., Miraflor, R. M. C. & Mungal, M. G. 1999 Direct measurement of entrainment in reacting/non-reacting turbulent jets using PIV. In *Intl Symp. on Turbulence and Shear Flow Phenomena.*

Hasselbrink, E. F. 1999 Transverse jets and jet flames: Structure, scaling, and effects of heat release. PhD thesis, Mechanical Engineering Department, Stanford University.

Hasselbrink, E. F. & Mungal, M. G. 1998*a* Characteristics of the velocity field near the instantaneous base of lifted nonpremixed turbulent jet flames. In *Twenty-Seventh Symp. (Intl) on Combustion, Boulder, CO*. The Combustion Institute.

Hasselbrink, E. F. & Mungal, M. G. 1998*b* Experiments on the stabilization region of a nonpremixed methane transverse jet flame. *Western States Section/The Combustion Institute Spring Meeting, Paper* WSS/CI 98S-43.

Hasselbrink, E. F. & Mungal, M. G. 1998*c* Observations on the stabilization region of lifted nonpremixed methane transverse jet flames. In *Twenty-Seventh Symp. (Intl) on Combustion, Boulder, CO*. The Combustion Institute, Pittsburgh, USA.

Hasselbrink, E. F. & Mungal, M. G. 2001 Transverse jets and jet flames. Part 1. Scaling laws for strong transverse jets. *J. Fluid Mech.* **443**, 1–25.

Kalghatgi, G. T. 1981 Blowout stability of gaseous jet diffusion flames. Part II: Effect of cross-wind. *Combust. Sci. Tech.* **26**, 241–244.

Kamotani, Y. & Greber, I. 1972 Experiments on a turbulent jet in a cross flow. *AIAA J.* **10**, 1425–1429.

Kelso, R. M., Lim, T. T. & Perry, A. E. 1996 An experimental study of round jets in cross-flow. *J. Fluid Mech.* **306**, 111–144.

Kuzo, D. M. 1995 An experimental study of the turbulent transverse jet. PhD thesis, California Institute of Technology.

Law, C. K., Zhu, D. L. & Yu, G. 1986 Propagation and extinction of stretched premixed flames. In *Twenty-First Symp. (Intl) on Combustion*, pp. 1419–1426. The Combustion Institute, Pittsburgh, PA.

Lourenco, L. & Krothapalli, A. 1995 On the accuracy of velocity and vorticity measurements with PIV. *Exps. Fluids* **18**, 421–428.

Margason, R. J. 1968 The path of a jet directed at large angles to a subsonic free stream. *Tech. Rep.* TN D-4919. NASA.

Margason, R. J. 1993 Fifty years of jet in crossflow research. In *AGARD Symp. on a Jet in Cross Flow, Winchester, UK, AGARD CP*–534.

Moussa, Z. M., Trischka, J. W. & Eskinazi, S. 1977 The near field in the mixing of a round jet with a cross-stream. *J. Fluid Mech.* **80**, 49–80.

Muñiz, L. 2001 Particle image velocimetry studies of turbulent nonpremixed flames. PhD thesis, Stanford University.

Muñiz, L., Martinez, R. M. & Mungal, M. G. 1996 Application of PIV to turbulent reacting flows. In *Eighth Intl. Symp. on Applications of Laser Techniques to Fluid Mechanics, Lisbon, Portugal.*

Muñiz, L. & Mungal, M. G. 1997 Instantaneous flame-stabilization velocities in lifted jet diffusion flames. *Combust. Flame* **111**(1/2), 16–31.

Mueller, C. J. & Schefer, R. W. 1997 Coupling of diffusion flame chemistry to an unsteady vortical flowfield. *Western States Section/The Combustion Institute Spring Meeting, Paper* WSS/CI 97S-028.

Nichols, C. E. 1985 Experiments with solid particle seeding. In *Wind Tunnel Seeding Systems for Laser Velocimeters* (ed. W. W. Hunter & C. E. Nichols), *NASA CP* 2393, pp. 77–84.

Patrick, M. A. 1967 Experimental investigation of the mixing and penetration of a round turbulent jet injected perpendicularly into a transverse stream. *Trans. Inst. Chem. Engrs* **45**, 16–31.

Peters, N. 1984 Partially premixed diffusion flamelets in non-premixed turbulent combustion. In *Twentieth Symp. (Intl) on Combustion*, pp. 353–360. The Combustion Institute, Pittsburgh.

Raffel, M., Willert, C. & Kompenhans, J. 1998 *Particle Image Velocimetry, A Practical Guide*. Springer.

Rehm, J. E. & Clemens, N. T. 1999 The large-scale turbulent structure of nonpremixed planar jet flames. *Combust. Flame* **116**, 615–626.

Ricou, F. P. & Spalding, D. B. 1961 Measurements of entrainment by axisymmetrical turbulent jets. *J. Fluid Mech.* **11**, 21–32.

Ross, C. B. 1993 Calibration of particle image velocimetry in a shock-containing supersonic flow. Master's thesis, Florida State University, Tallahassee.

Ruetsch, G., Vervisch, L. & Liñan, A. 1995 Effects of heat release on triple flames. *Phys. Fluids* **7**, 1447.

Schefer, R. W. & Goix, P. J. 1998 Mechanism of flame stabilization in turbulent, lifted-jet flames. *Combust. Flame* **112**, 559–574.

Seitzman, J. M. & Hanson, R. K. 1993 Comparison of excitation techniques for quantitative fluorescence imaging of reacting flows. *AIAA J.* **31**, 513–519.

Smith, S. H. 1996 The scalar concentration field of the axisymmetric jet in crossflow. PhD thesis, Stanford University.

Smith, S. H. & Mungal, M. G. 1998 Mixing, structure and scaling of the jet in crossflow. *J. Fluid Mech.* **357**, 83–122.

Sung, C. J., Law, C. K. & Axelbaum, R. L. 1994 Thermophoretic effects of seeding particles in LDV measurements of flames. *Combust. Sci. Tech.* **99**, 119–132.

Sykes, W., Lewellen, W. & Parker, S. 1986 On the vorticity dynamics of a turbulent jet in a crossflow. *J. Fluid Mech.* **168**, 393–413.

Takagi, T., Shin, H.-D. & Ishio, A. 1981 Properties of turbulence in turbulent diffusion flames. *Combust. Flame* **40**, 121–140.

Urban, W. D. 1999 Planar velocity measurements in compressible mixing layers. PhD thesis, Stanford University.

Westerweel, J. 1993 Analysis of PIV interrogation with low pixel resolution. In *Optical Diagnostics in Fluid and Thermal Flow, San Diego, CA. SPIE*–2005.

Westerweel, J. 1997 Fundamentals of particle image velocimetry. *Meas. Sci. Tech.* **8**, 1379–1392.

Westerweel, J., Dabiri, D. & Gharib, M. 1997 The effect of discrete window offset on the accuracy of cross-correlation analysis of digital PIV recordings. *Exps. Fluids* **23**, 20–28.

Wygnanski, I. & Fiedler, H. 1969 Some measurements in the self-preserving jet. *J. Fluid Mech.* **38**, 577–612.

Yuan, L. L., Street, R. L. & Ferziger, J. H. 1999 Large eddy simulations of a round jet in crossflow. *J. Fluid Mech.* **379**, 71–104.